Experimental Prediction of the Fracture of 6XXX Aluminum Alloys

by

Jackie Ayoub

A thesis submitted in partial fulfillment
of the requirements for the degree of
Master of Science in Engineering
(Industrial and Systems Engineering)
in the University of Michigan-Dearborn
2018

Master's Thesis Committee:

      Professor Ghassan Kridli, Co-Chair
      Andrey Ilinich, Ford Motor Company, Co-Chair
      Associate Professor Abdallah Chehade
      S. George Luckey, Ford Motor Company

Acknowledgements

Table of Contents

Table of Figures

List of Tables

Abstract

The fracture behavior of Al-6DR1 sheets during the stamping process is of specific importance in the automotive industry. Efforts were made to reduce the costs associated with fracture prediction by using numerical simulations instead of experimental testing. The motivation for developing the fracture surface is to improve the prediction of fractures in simulation that then can be used to guide the stamping/forming tool design process.

The theoretical framework employed in this thesis is based on two fracture models to predict the material behavior: The Modified Mohr-Coulomb (MMC) and the Hosford-Coulomb (HC). Furthermore, a hybrid and a direct calibration method are used to get the models parameters. The hybrid method is based on a numerical-experimental approach to get the variation of triaxiality and lode angle during deformation and it is also coupled with a damage accumulation rule. While the direct calibration method is based on a pure experimental approach, where the triaxiality on lode angle were assumed to be constant for the suggested experiments all the way to the fracture initiation stage. The specific tests used in the direct calibration are hemispherical punch stretching tests to induce equi-biaxial strain, pure shear tests, 3- point bend tests and Marciniak tests to induce plane strain, and hole-expansion tests to induce fracture under uniaxial tension strain.

To capture the effects of stress triaxiality and lode angle experienced in the material fabrication process, a range of stress states including was needed including pure shear, uniaxial tension, plane strain tension and equi-biaxial tension. The generated fracture surface is then validated and incorporated in numerical models that simulate the deformation process and allow for prediction of critical locations part locations that are likely to fracture during forming. Such predictive capabilities are important in the tool design stage.

Chapter 1: Introduction

1.1 Literature review

Aluminum is the fourteenth most abundant element on Earth by mass. It is extracted from the mineral bauxite. Pure aluminum is known to be ductile, soft and corrosion resistant. Thus, alloying aluminum with Cu, Zn, Mg, Si, Mn, and Li is necessary to enhance its strength properties, where Mg and Si are responsible for increasing the strength while Cu is added for better precipitation kinetics (Pogatscher et al., 2012). Aluminum alloys are classified into series (1000 to 8000 series) depending on the major alloying elements used. Certain aluminum alloy series are age-hardenable, including the 6000 Al-Mg-Si alloy series investigated in this thesis.

The use of aluminum (Al) in the automotive industry has been growing in the last 40 years due to many benefits such as its recyclability, energy efficiency, and high-strength-to-weight ratio. Aluminum is now considered the second most used material in vehicles after steel and research has shown that by replacing steel by aluminum in body-in-white (BIW), a 50% weight saving can be achieved (Miller et al., 2000). It was proven that an improvement of 5.5% in fuel economy can be achieved by a 10% decrease in vehicle weight (Miller et al., 2000). Table 1.1 shows the distribution of aluminum in different components of a European car.

Table1.1: Aluminum distribution in a European car (Hirsch, 2014)

Car components	Aluminum weight(Kg)
Car Body (doors, hoods, BIW, and bumpers)	26
Power-train (engine, liquid lines and fuel system)	69
Chassis and suspension (axle, wheels, steering system)	37

Determining the right alloy for the right vehicle component has been the focus of the automotive industry with the aim of achieving a balance between formability and strength. Thus, different aluminum alloys are used in different car components, for example Al6000 (Al-Mg-Si alloy) series is used in external body panels due to formability, its ability to achieve a class A-surface, its corrosion resistance and its welding capability.

Formability of Al alloys, measured by total elongation to fracture, is generally lower than low carbon steels. In particular, post necking strains in aluminum alloys are significantly lower than those of low carbon steel. Thus, the ability to predict fracture under the different modes of deformation experienced in stamping, is of greater interest by automotive designers.

Zhong et al. (2014) studied the effect of alloy composition and heat treatment on Al 6xxx series. It was found that increased Si content and decreased Mg/Si improved tensile ductility and stretch formability. They also reported that another way of achieving these property enhancements was by including 0.3% Cu to the alloys. Furthermore, pre-aging was noted to result in a decrease in strength, ductility and formability.

Dorbane et al. (2015) studied the effect of strain rate and temperature on Al 6061 alloy. They showed that the strain to fracture and the yield stress were both affected by a change in temperature and strain rate. In addition, they reported that increasing strain rate and decreasing temperature led to an increase in the yield strength and a decrease in the strain to fracture. To better understand the fracture mechanism, they tracked the progression of cracks at the microstructure level. It was found that cracks initiated between iron rich phases and that the initiation of cracks increased with temperature.

In order to improve the prediction of the deformation behavior of metal alloys, Hill (1948) developed an extension to von Mises quadratic yield criteria, which, until then, had depended only on deviatoric stresses. However, Hill's criterion was not able to predict the mechanical behavior of ductile materials since high plastic deformation would localize in a critical area prior to fracture for materials that fracture in a ductile manner.

Ductile fracture is characterized by the following 4 steps: (1) nucleation of micro voids due to second phase inclusions or pre-existing voids in the material, (2) void growth under the presence of applied forces, (3) plastic localization and coalescence at critical voids and (4)

rupture at the critical voids. Figure 1.1 is an illustration of a gradual damage accumulation where the slope change at point (A) is due to crack initiation caused by the coalescence of the largest voids.
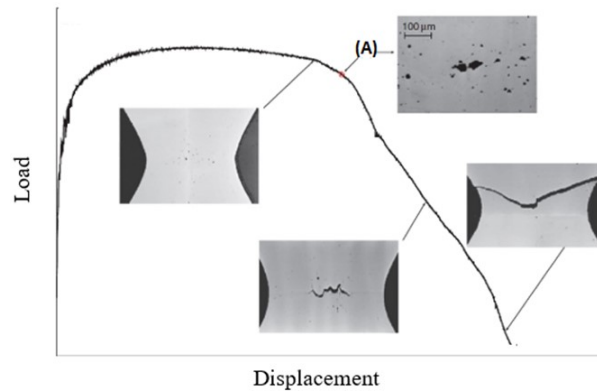
Figure 1.1: Illustration of ductile fracture of steel using the force versus displacement of a round notch specimen.(Benzerga, 2002)

Several models to analyze and predict the ductile fracture experienced by aluminum alloys have been reported in the literature. Rice and Tracey (1969) proposed a model to predict ductile fracture based on the growth of spherical voids. Gurson (1977) suggested a coupled damage model for porous materials and he set the mathematical fundamentals of porous plasticity where he assumed voids to be spherical and to stay spherical during deformation. Furthermore, Needleman and Tvergaard (1984) developed a model to describe the fracture process by analyzing void nucleation, growth, coalescence and finally the formation of cracks. Lemaitre (1992), presented a phenomenological method based on a damage parameter coupled with a thermal dissipation potential to describe the evolution of damage. Bai and Wierzbicki (2010) presented a new form of the Mohr-Coulomb criterion that is dependent on the stress triaxiality and Lode angle. The model uses the effect of these two parameters on the fracture behavior of ductile material and, subsequently, predicting the onset of fracture. Stress triaxiality is defined to be the ratio of the mean stress to the mean effective Mises stress.

Walter Lode was the first one to emphasis the importance of Lode angle in 1925. The influence of lode parameter on void evolution was studied by Zhang, 2001, who demonstrated that stress triaxiality was responsible for void deformation shape, but alone could not define a stress state that led to void growth and coalescence. Thus, the combination of stress triaxiality

3

and Lode parameter were used to describe void growth and coalescence. Wierzbicki et al., 2005 observed, in their experimental studies, that triaxiality was insufficient to characterize fracture in ductile material. Barsoum and Faleskog, 2011 showed that the lode parameter had a strong effect on void growth and shape and that this effect increased with decreasing the level of stress triaxiality.

Rice and Tracey (1969) and Agrawal et al. (2003) showed that void growth was strongly affected by the hydrostatic pressure. Both of these two studies concluded that fracture was due to prominent levels of stress triaxiality. A series of interrupted tests on notch radius specimens was performed by Agarwal et al. (2003) at distinct locations moving from the center to the edge. Tests results showed that the stress triaxiality is low at the edge of the specimen and high at the center, whereas for plastic strain the highest value was at the edge and the lowest at the center. Consequently, to understand the dependence of void growth and triaxiality, they performed microstructure analysis, where they saw that the deformation is localized near the Fe particles where triaxial stress state is dominate. Furthermore, stress triaxiality and equivalent plastic strain are noticed to be important on void growth but does not affect voids nucleation.

The aforementioned models that were developed to predict ductile fracture may be classified into three types: Gurson-type models, Mohr-Coulomb type models, and continuous damage mechanics type models. Following is a brief description of each type of fracture prediction models.

A) <u>Gurson type models</u>

In 1977, Gurson developed a model that set the mathematical fundamentals of porous plasticity. This void growth model assumed voids to be spherical and to stay spherical during loading. However, Gurson's model did not consider void coalescence. Needleman and Tvergaard (1984) noticed that with increasing porosity, local stress levels remained low due to softening. Along with the use of the Gurson Type model, they added a phenomenological description of void coalescence, considering two new parameters: critical porosity and acceleration rate. Still, the dependency of critical porosity and acceleration rate to the microstructure was missing in their model. Benzerga (2002) built on Needleman and Tvergaard's model to account for anisotropy. Benzerga defined ductile fracture to be dependent on void nucleation and void growth until coalescence. He developed a model with a set of constitutive equations to account

for the effect of coalescence and anisotropy of void shape and distribution.

B) Continuous Damage Mechanics Model

Lemaitre (1992), presented a phenomenological method based on a damage parameter coupled with a thermal dissipation potential to generate the evolution of damage. He described damage as a "debonding of atoms, and the accumulation of damage in the material at the mesoscale and microscale level to result in growth and coalescence of microcracks, leading to the formation of a crack at the microscopic level."

C) Mohr-Coulomb Model

Bai and Wierzbicki (2008) introduced another approach for predicting ductile fracture based on the modified Mohr-Coulomb criteria. Bai's approach took into consideration different stress states and the effect of triaxiality and lode angle. Moreover, the approach considered shear stress fracture criteria and modeled the direction of the plastic flow using an associated flow rule. The strain hardening behavior was obtained from uniaxial tension tests and was coupled with a power law fitting to extend the range of strain.

Modeling aluminum sheets is challenging, because they manifest anisotropy in their plastic response and fracture. Accordingly, Dunand et al. (2012) built on Barlat's Yld2000-2d criterion by adding an associated flow rule and an isotropic flow rule. In addition, a transformation from two-dimensional yield plane stress to three-dimensional stress state was presented in their work. Barlat et al. (2003) showed that to account for anisotropic yield, stress tensors needed to be converted in the isotropic yield function using two linear transformations on the Cauchy stress tensor. Furthermore, Dunand et al. (2012) presented the results of their experimental investigation on AA6260-T6, showing that the equivalent plastic strain was dependent on material orientation. Moreover, microstructure analyses did not show any dependency of fracture on second phase particles and the anisotropy was due to the formation of shear bands, which affect texture and grain arrangement.

Efforts have been made in the automotive industry to predict ductile fracture of aluminum 6xxx series by replacing experimental testing with numerical simulations to reduce time, money and to improve fracture prediction. The aim of this thesis is to investigate the ductile fracture of aluminum sheets and extruded tubes using two methods: an experimental-

numerical approach and a pure experimental approach. The outcome of the work is a fracture surface capable of predicting the onset of fracture of Al6DR1 alloy to improve simulation-based designs. A series of experiments are conducted to provide the needed stress state range to calibrate the fracture models.

1.2 Thesis objectives

The main objective of this thesis is to build the fracture surface for AL6DR1sheets. Accordingly, the goals of the study are:

1. To experimentally investigate the effect of material anisotropy and the state of applied stress on ductility and fracture.
2. To propose a series of linear strain path tests that can be used for direct experimental fracture model calibration.
3. Compare the outcome of two different fracture models namely modified Mohr-Coulomb (MMC) and Hosford-Coulomb(HC).
4. Compare the experimental and the hybrid calibration approach to predict fracture.

1.3 Thesis outline

This thesis consists of five chapters and are described below:

Chapter One is an introductory chapter that includes the thesis objectives and a literature review discussing the importance of aluminum in automotive industry, material properties of aluminum and the three existing models to predict ductile fracture.

Chapter Two provides a detailed explanation of the experimental procedure utilized, presents the studied material and the specimens geometry and finally the experimental results are presented and discussed.

In, **Chapter Three** the framework of the anisotropic plasticity model used in the numerical simulation is presented, a detailed comparison between experimental and simulation results is conducted.

Chapter Four presents the theoretical framework of the two fracture models (MMC and

HC), the model parameters calibration procedure and finally, the fracture prediction results are compared with the experiments and discussed.

And finally, **Chapter Five** summarize our contribution in this study by providing a comparison between the two studied fracture methods and finishing with concluding remarks and suggestion for future research.

Chapter 2: Experimental Procedure and Results

In this chapter, the experimental method used for the measurement of the load, displacement, and local strains are presented. The details of how the strains were extracted using the Digital Image Correlation (DIC) system are presented. Different specimen geometries were used to characterize the mechanical and fracture behavior of the investigated material. These geometries map a number of stress states that lead to different fracture limits. Furthermore, the specimens were machined with different orientations relative to the rolling direction of the material to characterize the anisotropic mechanical and fracture properties.

2.1. DIC calibration procedure

The DIC system is a powerful tool that follows the displacement of patterns located at the surface of a specimen. Using those displacement fields different type of strains can be calculated (local or global strains). Digital Image Correlation (DIC) is an analysis tool used to measure deformation, displacement and strain by evaluating a sequence of images. The DIC software (ARAMIS) recognizes the surface of the tested specimen and assigns coordinates to the image pixels. The default setting in ARAMIS uses the first image (undeformed specimen) as the reference image. The DIC tool can be connected directly to the machine controller in order to associate the measured force with the strains.

In this study, the DIC tool was used to integrate the force and cross-head displacement with the major and minor strains in the tested specimens. Deformation was computed based on comparisons between the reference image and the current image. Utilization of the DIC tool started by calibrating the system according to the manufacturer recommended procedure. The calibration procedure should ensure achieving the following:

- Calibration deviation between 0.015 and 0.075.
- Camera angle between 10º and 40º with the optimum value being 25º.

After calibrating the system, the distance between the left and right cameras should not be changed, and the distance between the cameras and the specimen should be maintained constant during testing.

The test specimen preparation for testing with the aid of a DIC systems required the specimen to be first cleaned with acetone to remove surface dirt and residual mill oil. This was done to ensure proper adhesion of the paint. During cleaning, the specimen was also checked for damage in the form of major scratches. Next, the width and thickness of the critical region of the specimen were measured. The specimen was then set under the paint hood for painting. A thin layer of white paint was first applied to the specimen surface and the paint was allowed to dry for few minutes. Speckles of black paint were applied over the white painted surface. It should be noted that for best test results, the consistency of quality of the painted surface is critical. This could be achieved by rigorously shaking the paint cans prior to spray painting the specimen. Also, it was noticed that there was a maximum elapsed time around 2 hours between painting and testing beyond which the paint started pealing, especially in the critical areas that experienced large deformation. This would result in missing critical fracture data.

Furthermore, the density and the size of the black paint speckles had to be carefully controlled as they were critical to the results. The speckle size also depended on the type of test and the specimen size. The size of the black speckles was controlled by the pressure applied on the spray nozzle as shown in figure2.1. The figure shows that different dot sizes were obtained with different nozzle pressures. For all tests performed in this study, the speckles size in pattern 4 was used (Figure 2.1). The exception was the shear specimen, which had a small critical region and experienced the most severe deformation. For the shear tests pattern 5 was used. When applying the black speckles, it was important to have 50% coverage of the surface; otherwise, the DIC would fail to capture the deformation zone adequately as it won't have sufficient contrast.
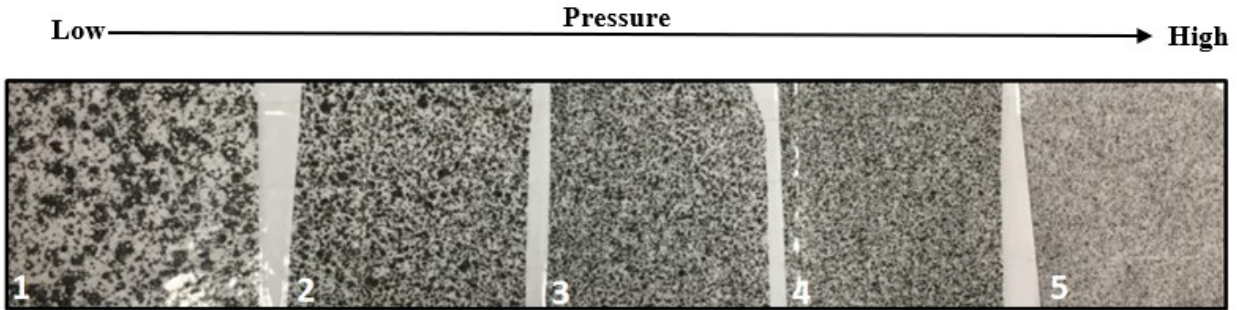
Figure 2.1: Variation of dot sizes with different nozzle pressures

2.1.1 Post processing of the DIC results corrected

Once testing was completed, the DIC results were processed. As mentioned earlier, the ARAMIS software detects the deformation by evaluating changes within facets. Each facet represents a measuring point.

A. Facet size and step

Two parameters related to the facets were used in the analysis of facet size and step. Facet size represented the number of pixels surrounding a node, as schematically shown in Figure 2.2. Facet size was used to calculate displacement at the center node. Facet step represented the spacing between two neighboring nodes. In his study, the Facet size was set as 11x11 pixels and the Facet step was chosen to be 7 pixels. It should be noted that the Facet size should always be higher that the facet step. A minimum Facet step of 5 pixels was recommended by the DIC manufacturer to reduce noise in the results.
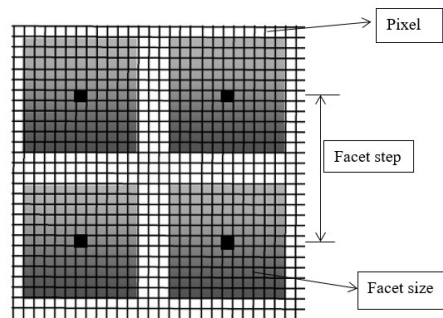
Figure 2.2: Illustration of Facet size and facet step in DIC

B. Selecting a starting point

After selecting the facet step and size, a required starting point was selected. A good starting point should be square and should be captured in the same position by both the left and the right cameras. Otherwise, the system calibration would need to be repeated. Once a starting point was selected the project computation could be performed.

C. Extracting the results

The DIC allows for obtaining a range of outputs. For example, the global force could be plotted versus the machine displacement. To extract the major and the minor strains, four stage points were chosen in the critical region, i.e. the region with the highest strains. A few examples are shown in Figure 2.3.

| (a) | (b) | (c) |
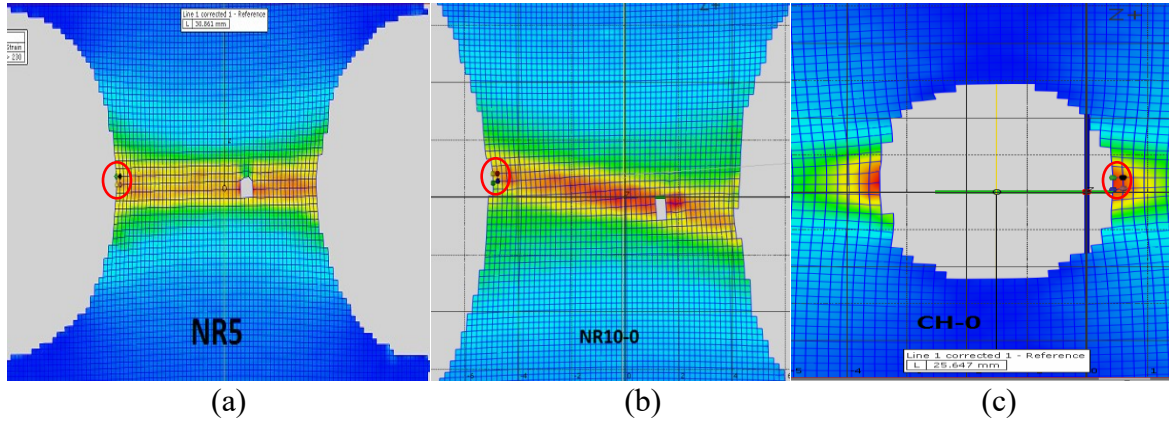
Figure 2.3: Highest strain points picked for different specimens: (a) NR5, (b) NR10 and (c) CH

The DIC tool computed three types of strains: engineering strain, Lagrangian strain and true (logarithmic) strain. Unless stated otherwise, the true strain was extracted from the DIC results. True strain was computed using equation 2.24:

$$\varepsilon_{true} = \ln(\lambda) = \ln\left(\frac{L}{L_0}\right) \qquad \textbf{2. 1}$$

2.2 Investigated specimen geometries

The experimental testing was performed on an MTS servo-hydraulic machine with a testing speed of 0.5 mm/min. The test specimens were machined from 1 mm Al-6DR1 sheets using a wire electrical discharge machine (EDM) in three different directions with respect to the rolling direction. All the specimens in this thesis were extracted with their major axis aligned with either of the rolling direction (RD), Diagonal Direction (DD), or Transverse Direction (TD)

as shown in figure 2.4. A DIC system was used for the strain measurements with the following setup characteristics:

Figure 2.4: Metal sheet directions along which he specimens were extracted

- A distance of 35 cm between the two cameras.
- A distance of 48.5 cm between the cameras to the specimen.
- An angle of 24.9° between the two cameras.
- A calibration deviation of 0.035 pixels.
- One images/second were captured for all the specimens except for shear where the rate of capturing images increased to 5 images/second at the stages close to fracture.

2.2.1 Uniaxial tension specimen (Dog-bone)

A uniaxial tension test specimen was used for the calibration of the plasticity model and for validating the fracture model. The shape and dimensions of this specimen type are shown in Figure 2.5. This specimen type is referred to as the DB specimen in this thesis. The loading is uniaxial strain until necking, beyond which the specimen develops plane strain loading. Figure 2.6 shows the force vs. displacement up to fracture exhibited by the three tested directions. Three specimens were tested in each sheet direction and Figure 2.6 shows the average force vs. displacement behavior. It is worth mentioning that the tests showed a very consistent repeatability. The three tested directions shows a very similar mechanical response. However, the displacement to fracture exhibited by the TD specimen is larger than the displacement to fracture exhibited by the RD and DD specimens as seen in figure 2.6. The difference in the displacement
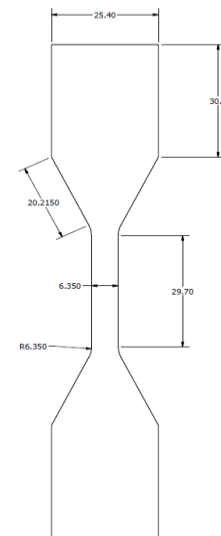
Figure 2.5: DB specimen dimensions (mm)

12

to fracture exhibited by the different specimen can be associated to the non-homogeneous shape of the grain structures that a rolled sheet of metal can present. Precisely, grains are usually observed to be elongated along the RD (Dorbane et al., 2015)

Figure 2.6: Force versus displacement for DB specimen at three different material orientations measured using DIC

2.2.2 Notch radius specimen

Notch radius specimens were used to generate a range of stress states through the variation of the radius R. When the width of the specimen increases, plane strain develops in the middle of the sample. Although, the edges develop uniaxial strain. Three different specimen geometries were used, and the geometrical features are presented in Figure 2.7. The notch radii were: R=5 mm, R=10mm and R=20mm. Three specimens were tested in each sheet direction and for each specimen geometries. A repeatable response was observed for each loading condition. The average force vs. displacement are summarized in Figures 2.8. It is observed that for each specimen geometry the three sheet directions exhibit the same elastic, yield and hardening behaviors. However, it is again observed that the RD displacement to fracture is the smallest when compared to other sheet directions. Furthermore, it is observed that by increasing notch radius of a specimen the deformation to fracture increase. In fact, decreasing the notch radius induces an increase of the stress concentration at the edge which will result in an earlier fracture.

13
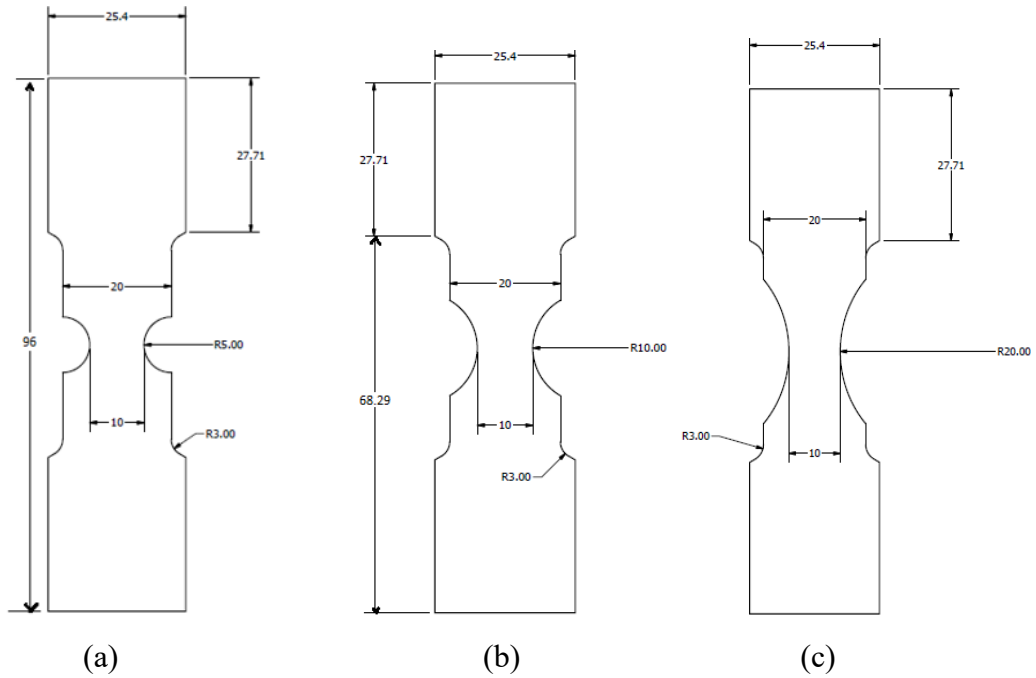
Figure 2.7: Notched radius specimens dimension (mm): (a) NR5, (b) NR10 and (c) NR20

(a)

(b)
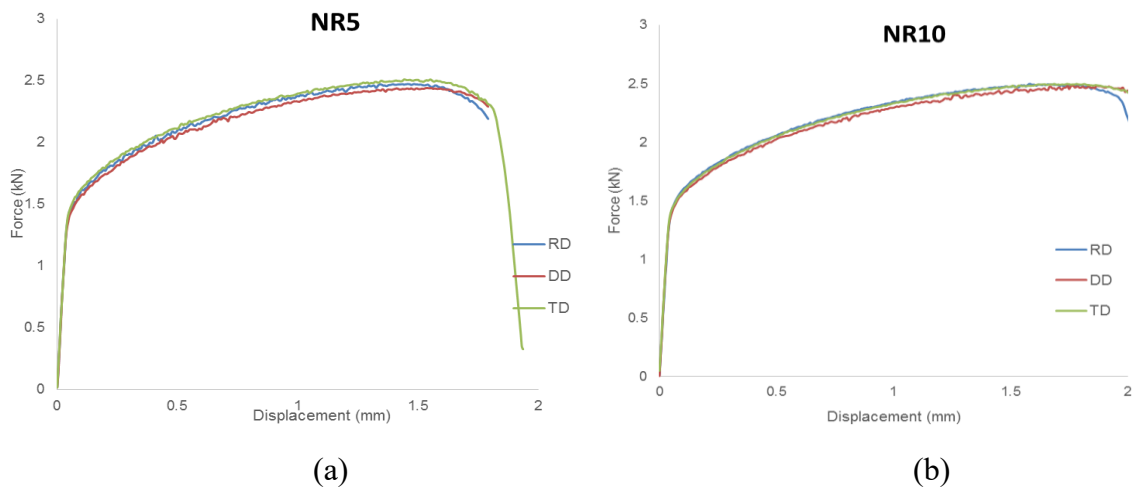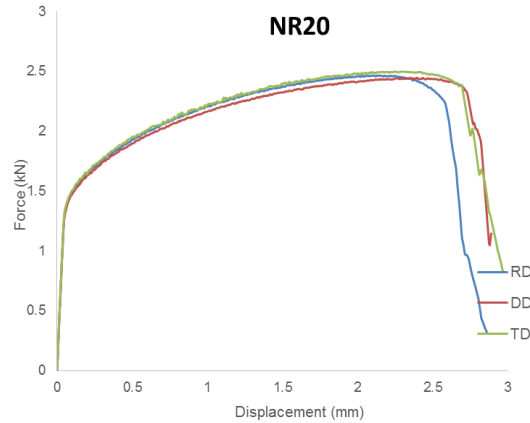
(c)

Figure 2.8: Force versus displacement for Notched radius specimens (a) NR5, (b) NR10 and (c) NR20 at three different material orientations measured using DIC

2.2.3 Central hole specimen

Central-hole specimens were used as an alternative to uniaxial tension specimens since the loading state didn't change during deformation. As mentioned earlier, the stress state in the uniaxial tension samples changes after necking from uniaxial strain to plane strain. For central-hole specimens, the free edge can always deform uniaxially. However, the large through thickness strain gradient in this type of specimen cannot be captured with DIC. The specimen geometrical features are presented in Figure 2.9. The specimen consists of a dog bone samples with a hole of 4 mm in diameter machined at its center. Three specimens were tested in each sheet direction. The results were again repeatable. The average force vs. displacement are summarized in Figures 2.10. It is observed that the three sheet directions exhibit very close mechanical behavior up to the point of fracture initiation.
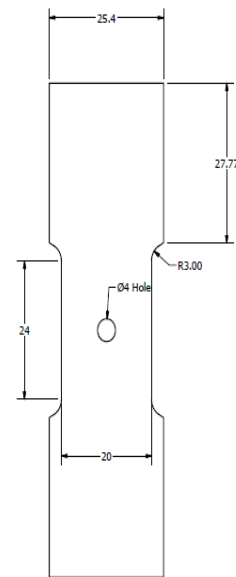
Figure 2.9: Central hole specimen dimensions (mm)
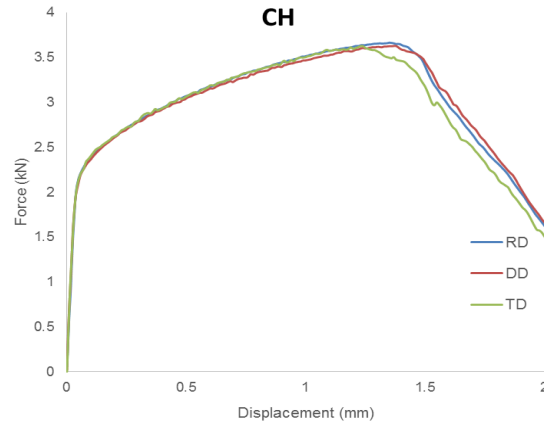
Figure 2.10: Force versus displacement for central hole specimens at three different material orientations measured using DIC

2.2.4 Shear specimen

The shear test specimens utilized in this study, were machined according to the geometry shown in Figure 2.11. The specimens were machine with their major axis aligned with the three sheet directions of interest. The measurement of the displacement field with DIC revealed to be very challenging due to the shape of the tested specimen that possesses unique characteristics. One of the issues encountered in this test was the apparent loss of DIC cameras focus during the early stages of deformation, prior to fracture initiation. It was initially thought that the loss of focus was caused by pealing of the paint due to severity of the deformation. However, upon further examination, it was determined that the issue was caused by the severity of

Figure 2.11: Shear specimen dimensions(mm)

the plastic deformation due to shear deformation in a relatively small zone, but there was no observed pealing of the paint.

16

| (a) | (b) |
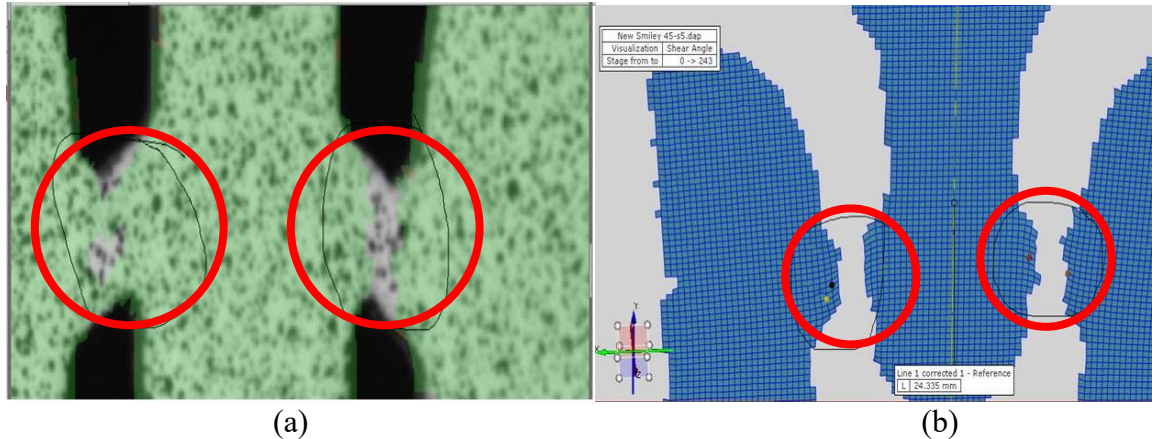
Figure 2.12: Critical regions in the shear specimens where DIC loses focus (a) DIC image snapshot (b) postprocessed image not showing results in the critical area

Since the speckle pattern was moving rapidly in this region, using the first stage as the reference stage led to the loss of focus. The issue was addressed using a moving reference stage such that for any stage (N) the reference stage was the previous stage (i.e., stage N-1).
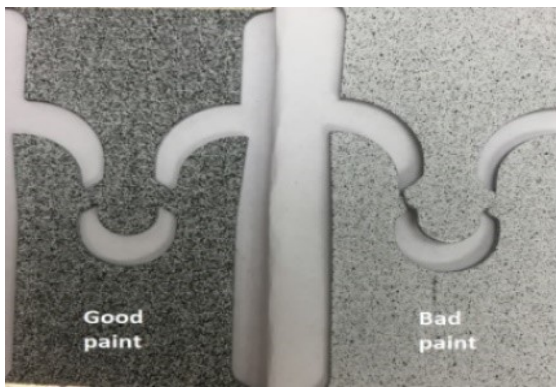
Figure 2.13: Paint improvement for a shear specimen

Additionally, the density of black speckles was increased in the critical region. Furthermore, the frequency of recording was increased for the later deformation stages as the point of fracture was approached. For example, from stage0 to stage150 one image per second was collected, and from stage150 till the fracture stage, five images per second were collected. This allowed for recording more images at the high deformation stages to get better results.

With two identical zones that experienced identical shear forces, failure occurred randomly in one of the two zones. Accordingly, it was determined to use two starting points (one in each zone) when conducting the shear test. Another issue that was encountered early in this study was related to the location of the DIC starting point. When fracture occurred, the fracture line separated the specimen into two sides: a side that contained the starting point and the other side. Accordingly, the DIC computed the strain only on that side of the test section that contained the starting point. To address this issue and have compute the strain in the other side of the

17

specimen, a second starting point needed to be introduced to this side of the fracture line during the stage immediately preceding the fracture stage.
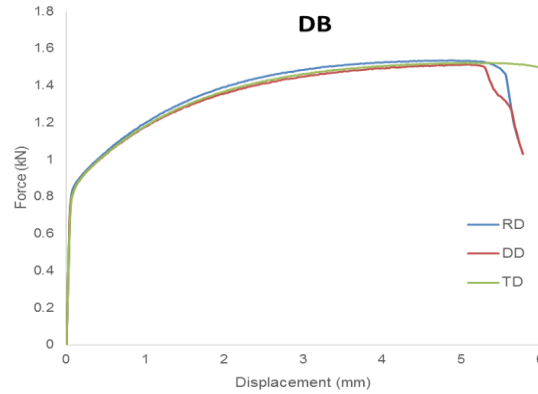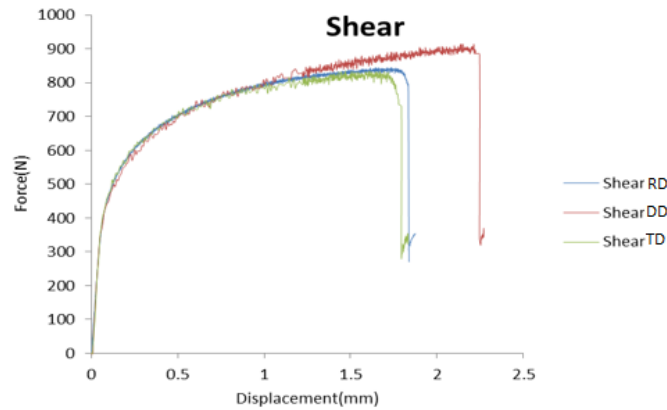

Figure 2.14: Force versus displacement for shear specimens at three different material orientations measured using DIC

Three specimens were tested in each sheet direction. The results were highly repeatable. The average force vs. displacement are summarized in Figures 2.14. It is observed that the three sheet directions exhibit similar mechanical behavior. The DIC results showed that shear specimens with their major axes machined along RD and TD directions had almost the same yielding and hardening behavior; however, the TD specimens experienced fracture at a lower displacement. Furthermore, the DD shear specimens showed a different hardening behavior than the RD and TD directions, and the displacement to fracture was significantly higher. It was noted that the shear specimens experienced deformation that resembled a pure shear stress state in the areas of interest. Considering a Mohr circle analysis approach, shear loading develops two equal principal stresses with opposite sign and with the principal directions oriented 45° with respect to the maximum shear plane. For instance, the shear specimen with their major axis aligned with the DD sheet direction develops a principal tensile and compressive stress along the RD and TD directions, respectively. The cracks developing along the RD direction are closed due to the compression stress developed along this direction, which can explain the higher strains to fracture. It can be argued that the same principal stress state is developed in the specimens with each of the specimen orientations; however, tensile loading along DD exhibited the highest displacement to fracture.

During deformation, and depending on the structure geometry, the blanks can experience

an evolving stress state (non-proportional loadings, evolving η and $\bar{\theta}$). Therefore, understanding the effect of stress state on the ductile fracture was the focus of many studies. Researchers worked on designing specimens that allow maintaining a constant stress state throughout the deformation to be used for validating their proposed fracture models for proportional loading. In sections 2.2.5, 2.2.6, and 2.2.7, three tests were developed to keep a constant stress state during the deformation up to fracture. The design details and the experimental results are provided in the following three subsections.

2.2.5 Plane strain test using Marciniak's test

The Marciniak test is generally used to generate the forming limit diagram (FLD) and has the advantage of using one tooling geometry with variable specimen geometries resulting in a variable strain loading conditions. The test is performed using a carrier blank (the blank is perforated with a circular hole at its center) that deforms with the blank to maintain a flat surface and eliminate bending. Instead of a hemispherical punch, a flat cylindrical punch is used. The hole in the carrier blank guarantees a free expansion of the blank resulting into a fracture initiating in the middle. The mechanics of the Marciniak test are shown in Figure2.15. When the well-lubricated punch moves up, the blank and the carrier blank are stretched outward. This leads to a strain concentration in the middle of the specimen and not at the edges of the punch as shown in figure2.15.
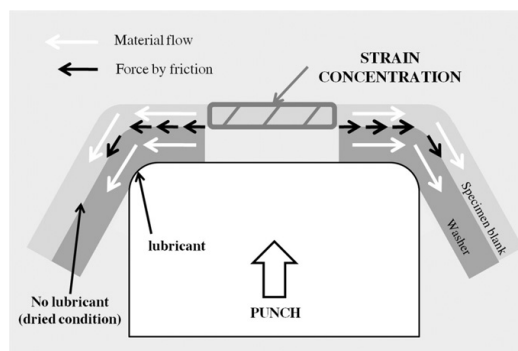
Figure 2.15: Marciniak test process.(Bong, Barlat, Lee, & Ahn, 2012)

This test was used to obtain the fracture limit under plane strain conditions. The proposed Marciniak testing device is shown in Figure2.16. The flat cylindrical punch had a radius of 50 mm and the device was designed to be inserted in an MTS hydraulic press. The AL6DR1 blanks

and the DDG steel blank carriers (Figure 2.17) were machined by water jet cutting

(a)

(b)

(c)
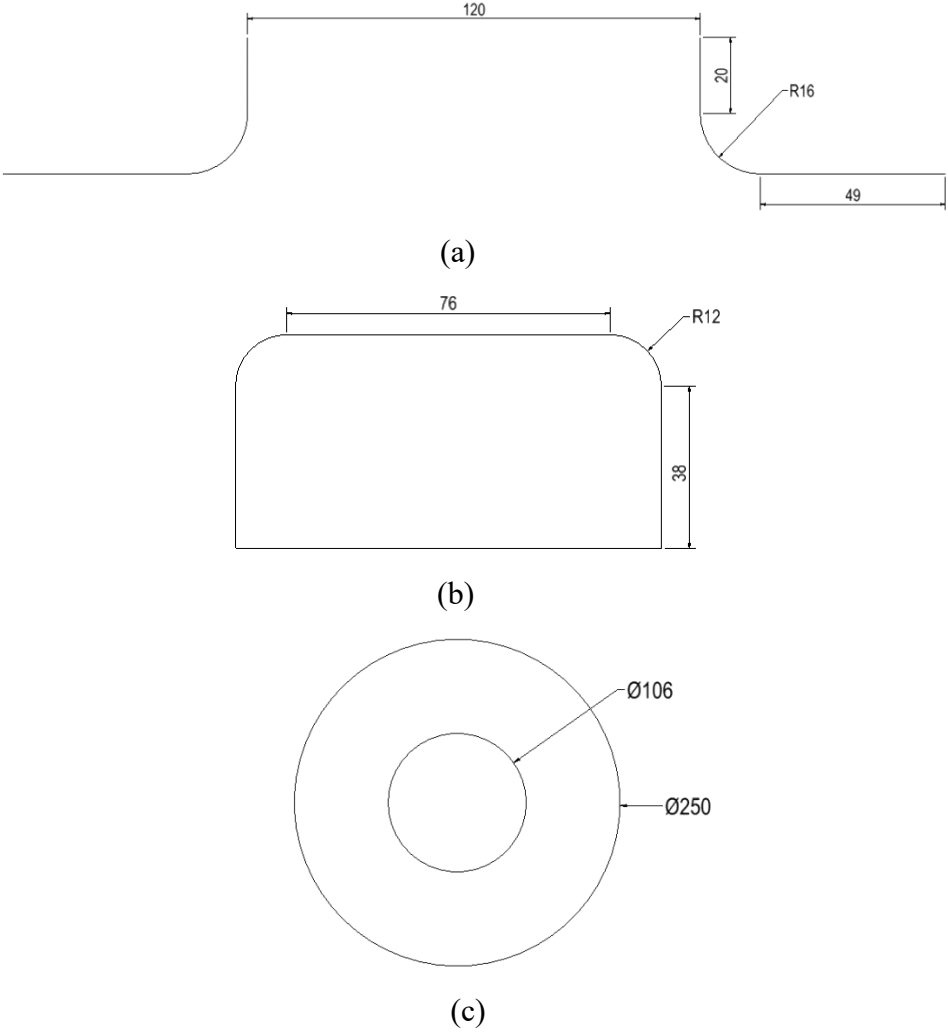
Figure 2.16:Drawings of Marciniak test components (a) Die (b) Punch (c) Holder
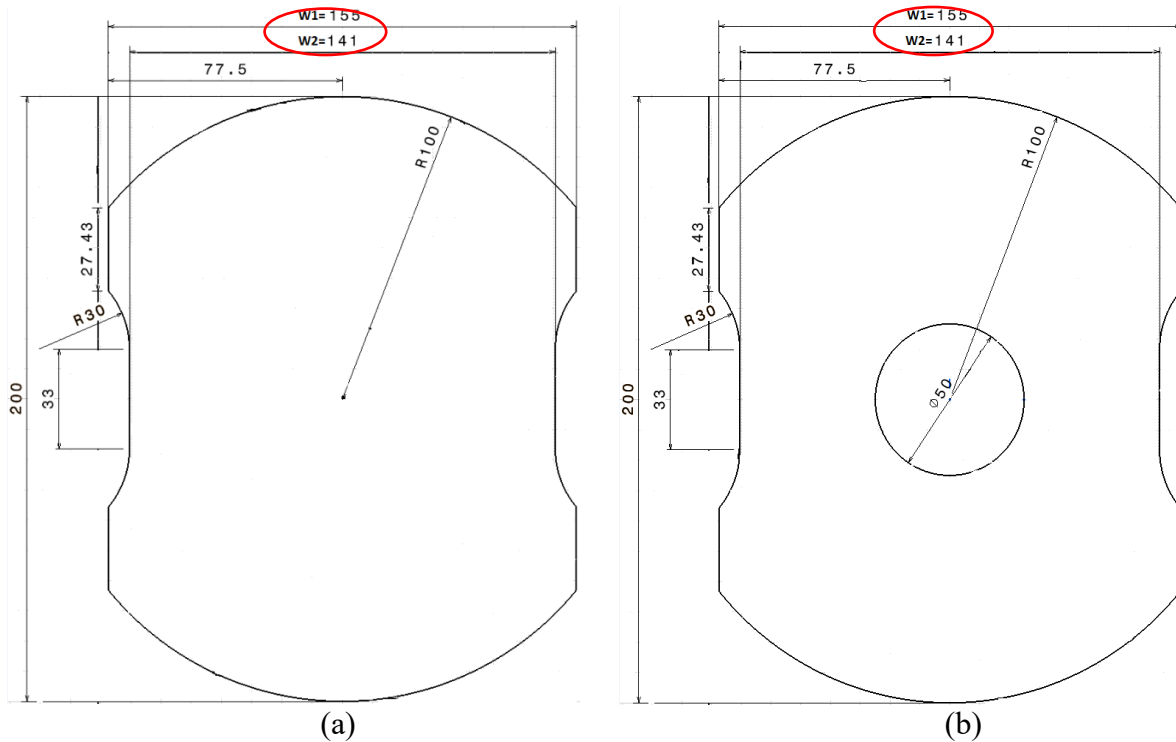
Figure 2. 17: Schematic of the geometry of (a) the Marciniak test Blank and (b) the Blank carrier

Since the test was performed using a closed die as shown in figure 2.18, in-situ strain measurement of the deforming blank surface using the DIC system was infeasible. Accordingly, the blanks were etched with a 2 mm diameter grid pattern prior to testing that were used for determining the major and the minor strains on the blank surface using the ARGUS system(figure 2.19). Lubricant QUAKER DRYCOTE 2-90 was used to lubricate the punch surface. The experiment was carried at a constant punch velocity until fracture was detected. ARGUS was used to measure the deformed grid dimensions in order to calculate the major and the minor strains.

Figure 2.18: Marciniak process

(a)   (b)
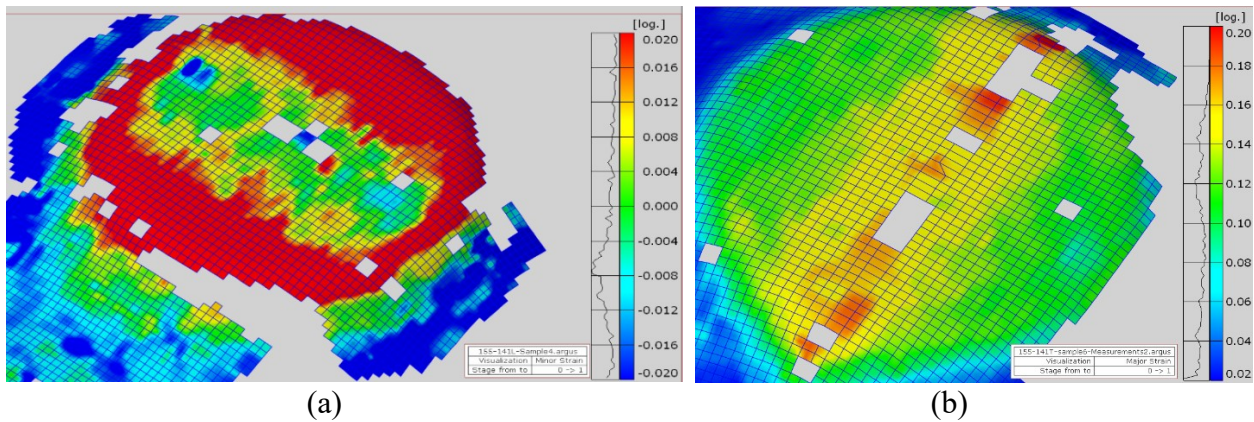
Figure 2.19: ARGUS (a) minor strain (b) major strain for 155-141 specimen

In order to achieve plane strain deformation, the surface minor strain should be minimized close to zero. Therefore, a sensitivity analysis was conducted to determine the effect of varying W1 and W2 on the minor strain (W1 and W2 are blank and carrier blank geometry

features as shown in Figure 2.17). The results of the sensitivity analysis are shown in Table 2.1. Accordingly, specimen with width1 (W1) = 155 mm and width2 (W2) = 141 mm were used for fracture analysis since these dimensions resulted in the smallest minor strain compared to all the other specimens. Table 2.2 presents the measured minor strains using ARGUS system. The minor strain is the strain measured in the parallel direction to the fracture line. It is verified that the minor strain stays close to zero for the different tested specimens. It is worth noticing that the Major strain defined as the strain along the perpendicular direction to the crack line can't be measured accurately in the critical area because of the strain localization.

Table 2.1: Minor strain measured with ARGUS for different combinations of W1 and W2 in L and T directions

Width1	Width2	Longitudinal	Transverse	Minor strain
145	136	X		-0.008
145	136		X	-0.005
155	141	X		0.004
155	141		X	0.003
157.5	143.5	X		0.008
157.5	143.5		X	0.006
160	146	X		0.005
160	146		X	0.006

Table 2.2: Global major and minor strain measured with ARGUS system for 155-141 AL6DR1 specimens in the longitudinal and transverse directions

ARGUS measurements	Minor strain
LD Sample1	0.008
LD Sample2	0.003
LD Sample3	0.005
LD Sample4	0.007
Average	0.00575
TD Sample1	0.004
TD Sample2	0.005
TD Sample3	0.006
Average	0.005

With the assumption of constant volume deformation when away from the necked region, the thickness strain should be equal to the surface major strain since the minor strain is equal to zero.

$$\varepsilon_{surface,major} + \varepsilon_{surface,minor} + \varepsilon_{thickness,major} = 0 \qquad\qquad \textbf{2. 2}$$

A Keyence VHX microscope was used to measure the thickness reduction to calculate the major strain at the necked region (critical area). For that purpose, specimens were sheared from the Marciniak specimen without damaging the critical region as shown in Figure 2.20. Three measurements were extracted with the microscope: in the center of the specimen (deformation occurred with the least friction) and two measurements of areas located at 2 cm away from the center. The results showed that the average major strain for specimens with their major axes in the RD and TD directions are almost the same. Table 2.3 lists the different tested specimens, the average measured thickness (of the three measured points) and the calculated major strain.

(a)

(b)
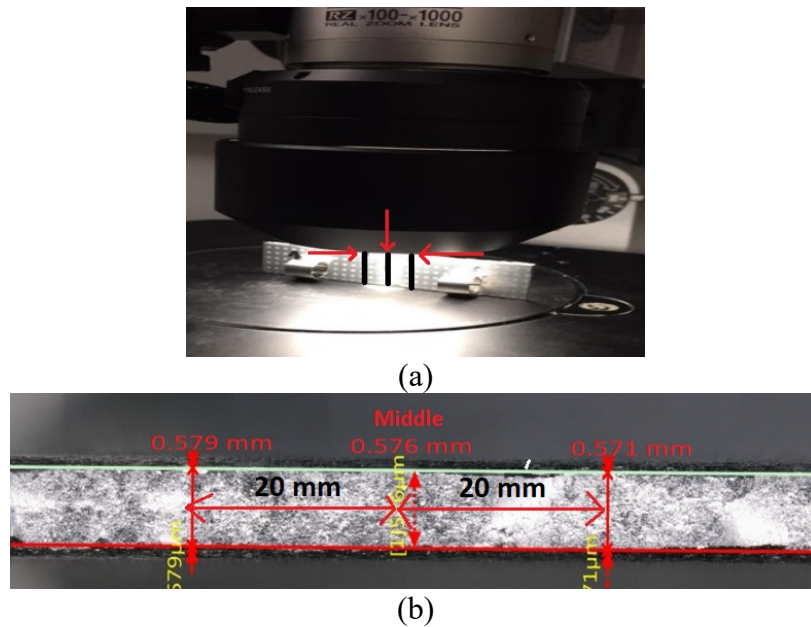
Figure 2.20: Keyence microscope thickness measurements: (a) measurement locations (b) measurement procedure

Table 2.3: Local major strain measured with Keyence microscope for 155-141 AL6DR1 specimens in the longitudinal and transverse directions

Keyence measurements	Thickness mm	Major strain mm/mm
LD Sample1	0.55	0.60
LD Sample2	0.54	0.62
LD Sample3	0.47	0.76
LD Sample4	0.51	0.67

Average		0.66
TD Sample1	0.56	0.58
TD Sample2	0.53	0.63
TD Sample3	0.46	0.78
Average		0.66

The results shows consistency with the ARGUS measurements, regarding the strain values being independent on the specimen major axis direction. An average major strain of 0.66 is found for the tested specimens with their major axis in the TD and RD directions. The Marcinak effective strains based on thickness strain measurements are the following:

$$\overline{\varepsilon}_{TD} = \frac{2}{\sqrt{3}}\varepsilon_{TD} = 0.765 \text{mm}/\text{mm} \qquad \textbf{2. 3}$$

$$\overline{\varepsilon}_{LD} = \frac{2}{\sqrt{3}}\varepsilon_{LD} = 0.762 \text{mm}/\text{mm} \qquad \textbf{2. 4}$$

2.2.6 Equi-biaxial tension test using a mini-punch

Motivated by the Erichsen cupping test, Roth and Mohr (2016) proposed a mini-punch device (Figure 2.21) for the purpose of measuring the equi-biaxial tension strain. For a better DIC vision, the fixture was designed in a way that allowed the entire fixture moved downward as the punch stayed fixed. The hole pattern machined in the blank was used for clamping the blank in the test fixture using bolts.

(a)   (b)

25

(c)   (d)
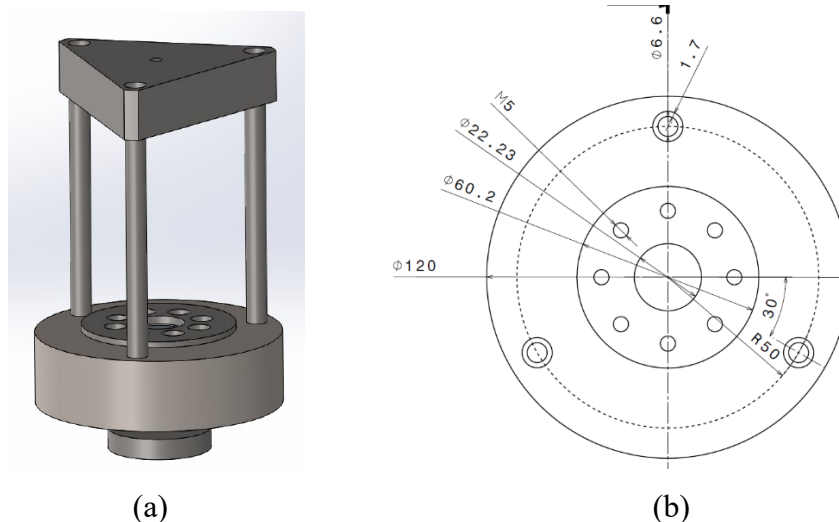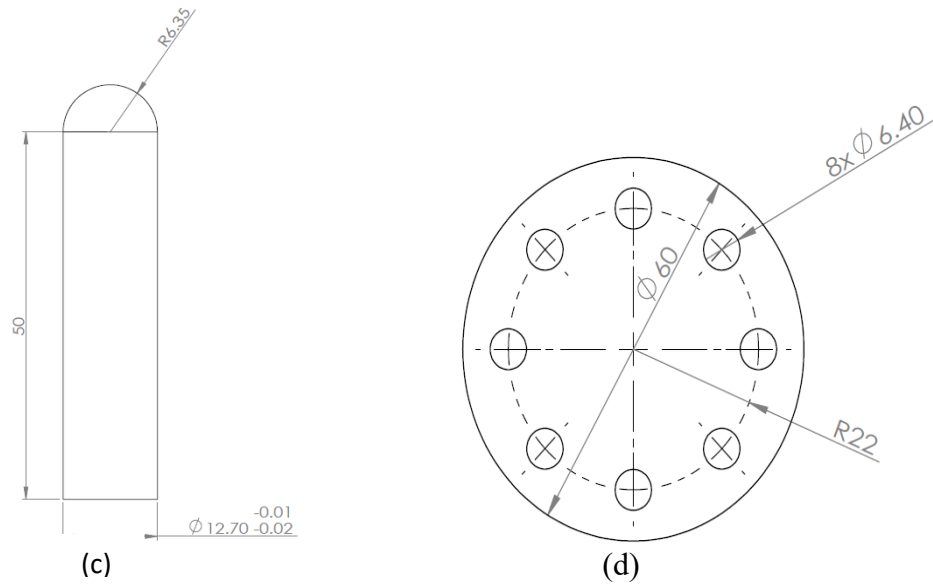
Figure 2.21: (a) photograph of a mini-punch testing fixture, (b) dimensions of the bottom fixture, (c) punch dimensions, (d) specimen dimensions

The mini-punch test was performed in a mechanical tensile machine (Instron4469) with 30 kN axial load cell and at a test rate of 2 mm/min. At the top of the punch, two small pieces of virgin Teflon with a 0.005" thickness were used to decrease friction. Major and minor strains were extracted using a digital image correlation system.
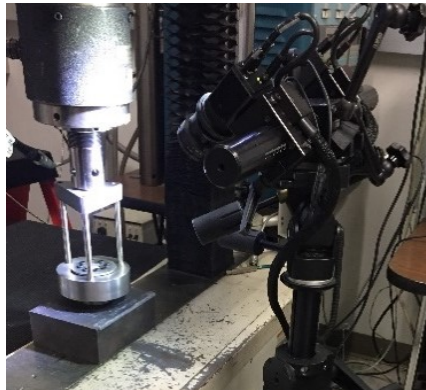
Figure 2.22: Photograph of the mini-punch fixture positioned in the testing machine with a DIC system

The reputability of the results was validated by conducting the mini punch test on four specimens up to the fracture initiation stage. The measured force versus displacement curve was observed to increase until the onset of fracture, where it suddenly dropped. Visual inspection of the fractured specimens showed that the fracture direction for the tested specimens was not along

the rolling direction (figure2.23(a)). The highest strain was noted to be localized in the apex of the dome in the deformed specimen (Figure 2.23 (b)). Accordingly, major and minor strains in the highest strain region were extracted from DIC (figure 2.24) at an average fracture initiation displacement of 7.7 mm. Then the effective plastic strain was calculated for each specimen as follow,

$$\overline{\varepsilon}_{effective} = \frac{2}{\sqrt{3}} \sqrt{\varepsilon_1^2 + \varepsilon_1 \varepsilon_2 + \varepsilon_2^2} \qquad\qquad 2.5$$

where ε_1 and ε_2 are the major strain and minor strains at fracture initiation. The average effective strain obtained was 0.86.

(a)   (b)
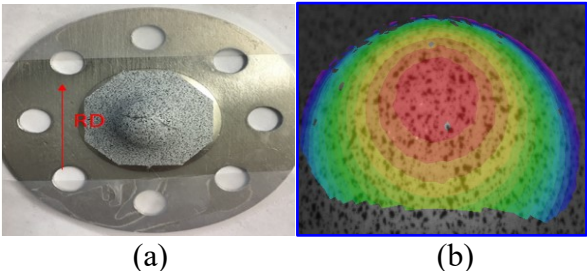
Figure 2.23: (a) Fracture of an AL6DR1 specimen, (b) Photograph of DIC strain distribution
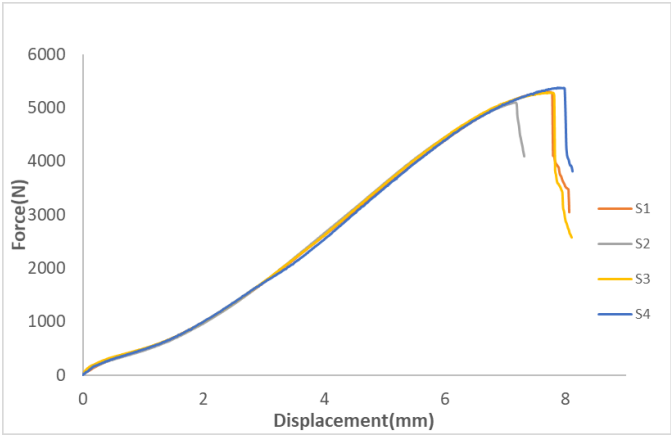
(a)
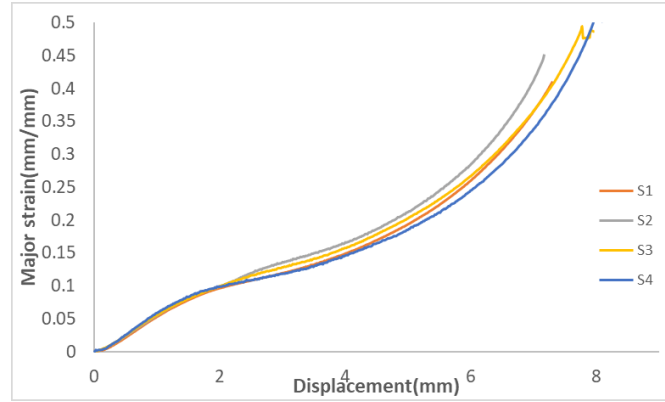
(b)
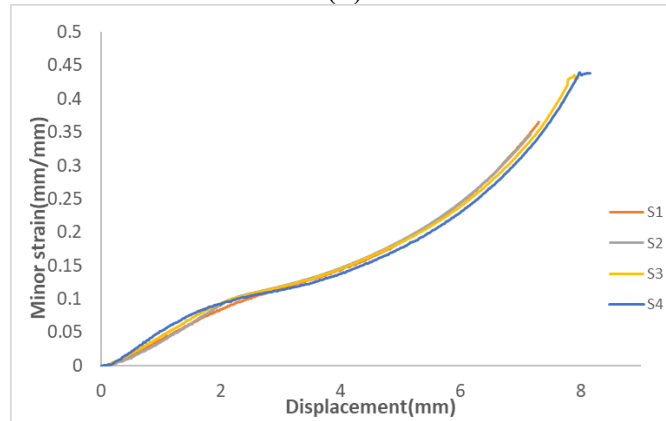
(c)

Figure 2.24: (a) Force, (b) major strain, (c) minor strain versus displacement for the tested specimens

2.2.7 Hole expansion

As discussed earlier, the extraction of strains in central hole experiments required the use of simulation. This is because the DIC system could only provide the surface strains while the most critical element in this test was at midpoint through the thickness. The hole expansion test was used since the stress state in the uniaxial tension test shifted to plane strain upon the onset of necking. Accordingly, the hole expansion test was used as a substitute for CH and DB tests since it experimentally provided the needed uniaxial tension strains to characterize the material ductility without the use of simulation.

In the hole expansion test, the fracture was observed to initiate at the hole boundary as can be seen in Figure 2.25. Through the thickness necking was not observed which might have

been the suppression of necking due to the strain gradient in the thickness. The strain gradient was observed to increase with increasing thickness and with decreasing radius. An increase in the strain gradient was observed to prevent necking and to allow for achieving a pure uniaxial tension strain on the edges of the hole

$$\text{strain gradient} = \frac{\text{Thickness}}{\text{Hole diameter}} \qquad\qquad \textbf{2. 6}$$
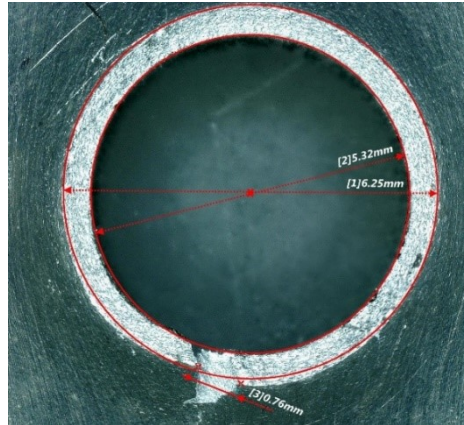
Figure 2.25: Hole expansion specimen with uniform deformation and no necking before fracture

The experiment was carried out using the same mini-punch fixture; however, the punch was replaced with a conical punch shown in figure 2.26b. A 3 mm diameter hole was machined at the center of the test specimen as can be shown in Figure 2.26a. Other specimen features were the same as those for the mini-punch biaxial test specimen. Specimens were machined of Al6DR1 sheet using a water jet cutting machine. The tests were conducted using an Instron electro-mechanical testing machine with a 10 KN load cell. The tests were conducted at a constant velocity of 4 mm/min until fracture initiation.
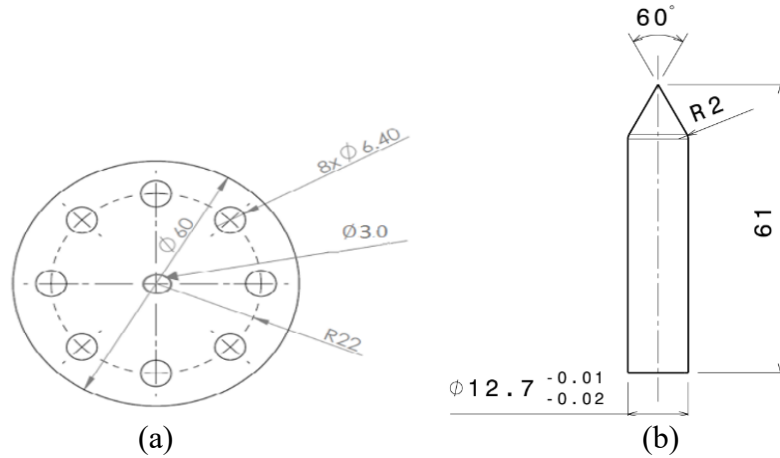
Figure 2.26:Hole expansion (a) specimen and (b)punch dimensions in mm

A Keyence microscope was used to measure the outer hole diameter and cracks length at fracture and then the outer hole diameter at fracture initiation was calculated as follow:

$$\textbf{Diameter}_{\textbf{fracture initiation}} = \frac{\pi \textbf{Diameter}_{\textbf{fracture}} - \sum \textbf{cracks width}}{\pi} \qquad \textbf{2.7}$$

An average strain of 0.78 mm/mm was obtained for the four tested specimens.

Chapter 3: Plasticity Model and Numerical Results

The main advantages of computer simulations are in reducing cost and time by modeling physical behavior. One application of computer simulations is in crash testing of vehicles. In the past, car companies had to destructively crash thousands of cars during the design process but with the help of crash simulations the study can take only a few minutes to gain valuable information. Millions of elements are included in a crash simulation model. These elements are assigned associated material properties like yield strength, hardening parameters and fracture criteria to enhance the accuracy of the simulation. Another application of material simulation exists in stamping processes, where simulations can help in predicting common defects like buckling, tearing and wrinkling so products can meet the needed quality requirements. Furthermore, simulations can help in optimizing the stamping tool design before the tool is manufactured.

Predicting the plastic behavior of aluminum alloys has been the focus of many researchers due to the high evolution of the local stress state throughout the changes in geometry of the tested specimen. In this work, a numerical simulation analyses using a material subroutine was used to predict the material behavior up to the point of fracture initiation. The obtained results are compared with the experimental results of Chapter 2.

3.1 Plasticity Model Theoretical Framework

The plasticity model in this thesis work is based on a Yld2000-3d criterion with an associated flow rule and an isotropic hardening to characterize the yielding and plastic behavior of AL6DR1. The mathematical formulation for this criterion was reported by Dunand et al. (2012) and is shown in Equations 3.1 through 3.13.

Accordingly, the yield surface f(α, k) was expressed as a function of the stress tensor in the plane stress state and a yield stress element obtained from swift hardening law:

$$f(\sigma, k) = \bar{\sigma} - k = 0 \tag{3.1}$$

With the component of the plane stress tensor $\boldsymbol{\sigma}$ being τ shear element, σ_x stress tensor in the elongation direction (ED), and σ_y stress tensor in the transverse direction (TD).

$$\bar{\sigma} = \frac{1}{2^{\frac{1}{a}}} \left(\left| S'_I - S''_{II} \right|^a + \left| 2S''_{II} + S''_I \right|^a + \left| 2S''_I + S''_{II} \right|^a \right)^{\frac{1}{a}} \tag{3.2}$$

where S'_I, S'_{II}, S''_I, and S''_{II} represent the principal values of the stress tensors that are described by the stress tensors $\boldsymbol{S'}$ and $\boldsymbol{S''}$. Two linear transformation of the stress tensors $\boldsymbol{S'}$ and $\boldsymbol{S''}$ are defined as follows,

$$\boldsymbol{S'} = \frac{1}{3} \begin{bmatrix} 2\alpha_1 & -\alpha_1 & 0 \\ -\alpha_2 & 2\alpha_2 & 0 \\ 0 & 0 & 3\alpha_7 \end{bmatrix} \begin{Bmatrix} \sigma_x \\ \sigma_y \\ \tau_{xy} \end{Bmatrix} \tag{3.3}$$

$$\boldsymbol{S''} = \frac{1}{9} \begin{bmatrix} -2\alpha_3 + 2\alpha_4 + 8\alpha_5 - 2\alpha_6 & \alpha_3 - 4\alpha_4 - 4\alpha_5 + 4\alpha_6 & 0 \\ 4\alpha_3 - 4\alpha_4 - 4\alpha_5 + \alpha_6 & -2\alpha_3 + 8\alpha_4 + 2\alpha_5 - 2\alpha_6 & 0 \\ 0 & 0 & 9\alpha_8 \end{bmatrix} \begin{Bmatrix} \sigma_x \\ \sigma_y \\ \tau_{xy} \end{Bmatrix} \tag{3.4}$$

where α_1, …. α_8 and exponent "a" represents the transformation coefficients of the anisotropic yield function, they are determined from experiments. When all α parameters are equal to 1 the material is isotropic (i.e. von Mises yield criteria).

The experimental data used for the calibration of the α parameters are: the uniaxial yield stresses in the three tested orientations Y_0, Y_{45}, Y_{90} , the r-values r_0, r_{45}, r_{90} and, from the shear test, the yield stresses τ_0 and τ_{45}.

Dunand et al. (2012) proposed the three-dimensional general stress state shown in equations (3.5, 3.6, and 3.7). These equations were developed as an extension of the Yld2000-2d plane stress criterion, taking into consideration symmetry with respect to X, Y, and Z directions.

$$\bar{\sigma} = \frac{1}{2^{1/a}} \left(\Phi'(\boldsymbol{S'}) + \Phi''(\boldsymbol{S''}) \right)^{\frac{1}{a}} \tag{3.5}$$

such that,

$$\Phi'\left(\mathbf{S'}\right)=\left[\left(S'_{xx}-S'_{yy}\right)^2+4\left(S'^2_{xy}+S'^2_{xz}+S'^2_{yz}\right)\right]^{\frac{a}{2}}$$

3. 6

$$\phi''\left(\mathbf{S''}\right)=\left[\frac{3}{2}\left(S''_{xx}-S''_{yy}\right)+\frac{1}{2}\sqrt{\left(S''_{xx}-S''_{yy}\right)^2+4\left(S''^2_{xy}+S''^2_{xz}+S''^2_{yz}\right)}\right]^{a}+\left[\frac{3}{2}\left(S''_{xx}-S''_{yy}\right)-\frac{1}{2}\sqrt{\left(S''_{xx}-S''_{yy}\right)^2+4\left(S''^2_{xy}+S''^2_{xz}+S''^2_{yz}\right)}\right]^{a}$$

3. 7

Where $\mathbf{S'}=\mathbf{L'}\sigma$, $\mathbf{S''}=\mathbf{L''}\sigma$ and $S'_{zz}=-\left(S'_{xx}+S'_{yy}\right)$, $S''_{zz}=-(S''_{xx}+S''_{yy})$

This transformation uses the same eight α parameters as the Yld2000-2d yield function and adds four other α parameters that are considered to have a value of 1 (one). The linear transformations of $\mathbf{L'}$ and $\mathbf{L''}$ are shown in Equations 3.8 and 3.9.

$$\mathbf{L'}=\frac{1}{3}\begin{bmatrix} 2\alpha_1 & -\alpha_1 & -\alpha_1 & 0 & 0 & 0 \\ -\alpha_2 & 2\alpha_2 & -\alpha_2 & 0 & 0 & 0 \\ 0 & 0 & 0 & 3\alpha_7 & 0 & 0 \\ 0 & 0 & 0 & 0 & 3\alpha_9 & 0 \\ 0 & 0 & 0 & 0 & 0 & 3\alpha_{10} \end{bmatrix}$$

3.8

$$\mathbf{L''}=\frac{1}{9}\begin{bmatrix} -2\alpha_3+2\alpha_4+8\alpha_5-2\alpha_6 & -4\alpha_4+4\alpha_6+\alpha_3-4\alpha_5 & \alpha_3+2\alpha_4-4\alpha_5-2\alpha_6 & 0 & 0 & 0 \\ 4\alpha_3-4\alpha_4-4\alpha_5+\alpha_6 & -2\alpha_3+8\alpha_4+2\alpha_5-2\alpha_6 & -2\alpha_3-4\alpha_4+2\alpha_5+\alpha_6 & 0 & 0 & 0 \\ 0 & 0 & 0 & 9\alpha_8 & 0 & 0 \\ 0 & 0 & 0 & 0 & 9\alpha_{11} & 0 \\ 0 & 0 & 0 & 0 & 0 & 9\alpha_{12} \end{bmatrix}$$

3. 9

To calibrate the first six alpha parameters, Barlat et al. (2003) suggested solving equation 3.10 for the stress state and equation 3.11 for R-values using the yield stress and lankford coefficients obtained from the uniaxial tension test and biaxial compression (σ_0 , $\sigma_{90}, \sigma_b, r_0, r_{90}$ and r_b):

$$F=\phi-2\left(\bar{\sigma}/\sigma\right)^a=0$$

3. 10

$$G=q_x\frac{\partial\phi}{\partial s_{xx}}-q_y\frac{\partial\phi}{\partial s_{yy}}=0$$

3. 11

where $\phi=\left|\alpha_1\gamma-\alpha_1\delta\right|^a+\left|\alpha_3\gamma-2\alpha_4\delta\right|^a+\left|2\alpha_5\gamma-\alpha_6\delta\right|^a-2\left(\bar{\sigma}/\sigma\right)^a=0$

33

And $s_x = \gamma\sigma, \ s_y = \delta\sigma$

Table 3.1 : q$_x$ and q$_y$ equations at different loadings

	q_x	q_y
Longitudinal tension (0°)	$1\text{-}r_0$	$2\text{+}r_0$
Transverse tension (90°)	$2\text{+}r_{90}$	$1\text{-}r_{90}$
Biaxial tension	$1\text{+}2r_b$	$2\text{+}r_b$

The values of the parameters α_7 and α_8 are obtained by solving equation 3.12 using the yield stress σ_{45} and R-value r_{45} in the diagonal direction of a uniaxial tension test:

$$F = \left|\frac{\sqrt{k_2'^2 + 4\alpha_7^2}}{2}\right|^a + \left|\frac{3k_1'' - \sqrt{k_2''^2 + 4\alpha_8^2}}{4}\right|^a + \left|\frac{3k_1'' + \sqrt{k_2''^2 + 4\alpha_8^2}}{4}\right|^a - 2\left(\bar{\sigma}/\sigma_{45}\right)^a = 0 \qquad \textbf{3. 12}$$

$$K_2' = \frac{\alpha_1 - \alpha_2}{3}$$

$$K_1'' = \frac{2\alpha_5 + \alpha_6 + \alpha_3 + 2\alpha_4}{9}$$

$$K_2'' = \frac{2\alpha_5 + \alpha_6 - \alpha_3 - 2\alpha_4}{3}$$

To calibrate the Yld2000-3d model, tension test and compression test measurements were used. Uniaxial tension specimens from a 1 mm thick sheet of AL6DR1 were machined using wire EDM and the tests were performed using an Instron servo-hydraulic universal testing machine. Digital image correlation was used to measure the major and minor strains in the gage section and to measure the load variation versus the gage displacement.

To quantify planar anisotropy of the Al-6DR1 alloy, Lankford ratios were calculated using uniaxial tension specimens, as being the slope of the absolute minor (width) strain versus the absolute thickness strain (Table 3.2).

Table 3.2: R-value obtained at different material orientations

Material orientation	0°	45°	90°
Average R-value	0.744	0.436	0.908

In addition, a through thickness compression was conducted on a disk of a 12.7 mm diameter and a 1 mm thickness using an Instron machine. Ten specimens were tested, each at a different load ranging from 30 to 90 KN. The thickness and diameter measurement were used to calculate the transverse and longitudinal strain in order to calculate the biaxial ratio r_b which was found to be equal to 0.8. The calibration results of Barlat's YLD2000-3d are shown in Table 3.3.

Table 3. 3: α_x parameters

α_1	α_2	α_3	α_4	α_5	α_6	α_7	α_8	$\alpha_{9.....12}$
0.93982	1.037227	0.92237	1.0073	1.02075	1.01343	0.939541	1.154943	1

The stress-strain curve of uniaxial tension specimens required extrapolation to higher strain levels to predict the onset of fracture. Therefore, a combination of Swift law and Hockett-Sherby law (Equation 3.13) was used to describe the hardening behavior.

$$\sigma = (1-\alpha)\left[c\left(\varepsilon_p + \varepsilon_0\right)^m \right] + \alpha\left[\sigma_{sat} - \left(\sigma_{sat} - \sigma_i\right)e^{-a\varepsilon_p^n} \right] \qquad \textbf{3. 13}$$

Where, σ represents the equivalent stress; α weighting coefficient (0.75); C is swift law parameter; a, m and n are hardening parameters of the Swift-Hockett-Sherby law; ε_p is the plastic strain; ε_0 is the pre-strain, σ_{sat} is the saturation stress and σ_i is the initial stress. The resulting stress-strain curve used in the simulation is presented in Figure 3.1.
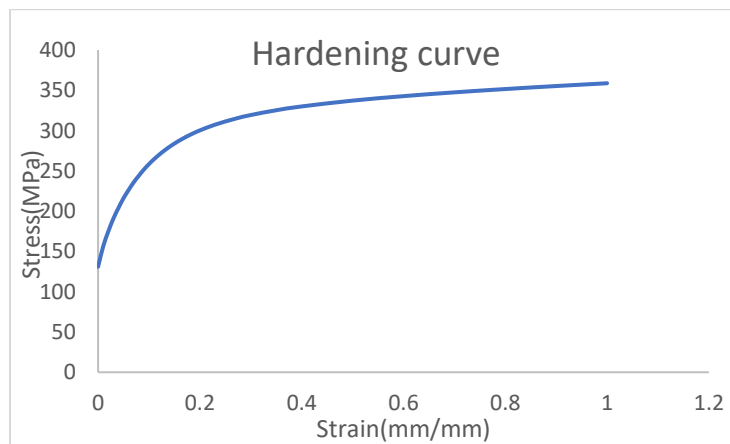
Figure3.1: Hardening curve used in the simulation

3.2 Numerical Simulations

3.2.1 ABAQUS Procedure

The DIC system can only provide strains on the surface of the tested specimen; however, calibration of the fracture model requires an understanding of the strains at the most damaged element, which may be through the thickness of the specimen. Therefore, a numerical simulation was used to determine this necessary information to calibrate the fracture model. ABAQUS/Explicit was used to simulate specimen deformation. The symmetry of the specimen allowed for the simulation of 1/8th of a specimen to reduce the amount of time for calculations (Figure 3.2).

Figure3.2: ABAQUS drawing of a 1/8 of an NR5 sample

In addition to geometry and material properties, the tested specimen orientation relative to the rolling direction of the sheet (i.e. 0°, 45° or 90°) was specified in the model. The convention used in the material subroutine was that axis "1" always referred to the rolling direction(RD). A solid homogeneous section was defined and then assigned to the part. To be able to compare the strain between the same deformation location in both ABAQUS and DIC, the mesh distribution in ABAQUS was set to match with the DIC mesh distribution. Accordingly, a square element with a size of 0.2 mm x 0.2 mm was set in the specimen gage section. At least 5 elements were meshed through the thicknesses. Partitions were added to the surface of the specimen, in order to have a uniform mesh distribution. A set of boundary conditions were applied to the specimen

Figure3.3: Set of boundary conditions used to limit the specimen movement from the top, left and bottom

as shown in Figure 3.3, to limit its movement from the bottom, left and the backside since

$1/8^{th}$ of a specimen was modeled. A velocity boundary condition of 10 mm/s was applied to the outmost elements in the modeled grip section. History output requests were used for the extraction of results to be compared with DIC results. Force was calculated as the summation of forces on a transverse plane. For the displacement, since it should match with the displacement chosen in DIC, a node was selected in the gage section having a length of half the gage length from the node to the bottom part of the specimen as shown in figure 3.4.

(a)   (b)
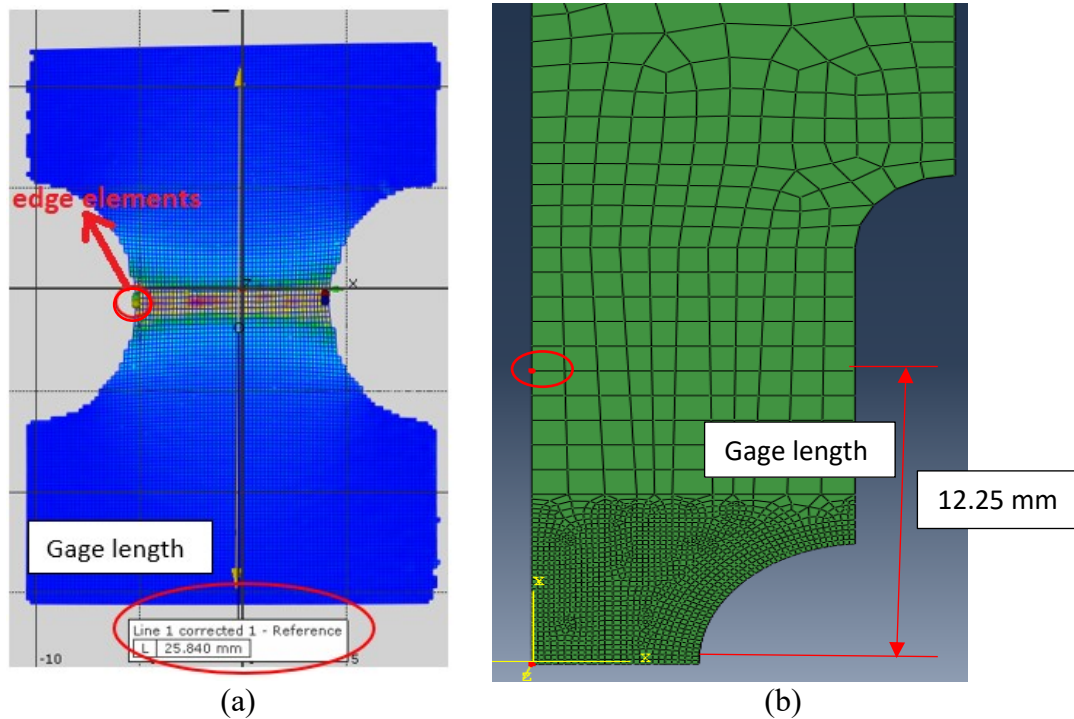
Figure3.4: Gage displacement length comparison between (a) DIC and (b) ABAQUS

Mass scaling is a tool that can be employed to increase the speed of the simulation without sacrificing solution accuracy. The idea of mass scaling is that the time step can be increased by scaling up the density in the smallest elements. Users indicate a minimum time step size of 0.2 s; any elements having a time step less than the specified one will have an increase in density until the time step reaches the specified value.

A mass scaling study was carried out to determine the maximum amount of mass scaling that could be used. The mass scaling study was performed on the specimen with notch radius of 5 mm specimen (NR5). Since the computation time increased with an increasing number of elements and a decreasing time step size, larger element sizes were meshed outside the critical

37

region (element size of 1 mm x 1 mm was used). ABAQUS simulation was run once without mass scaling and three other simulations were run at densities of $5.0e^{-6}$, $5.0e^{-7}$ and $5.0e^{-8}$. The simulation without mass-scaling required over 24 hours to compute the results; however, with each of the three tested levels of mass-scaling, the simulation runs were completed in about 30 minutes. The major and minor strains for the first edge element (figure 3.4(a)) were extracted and compared between for all tested simulation run. The results showed no difference in the strain results (Figures 3.5 and 3.6). Accordingly, a mass scaling with a density of $5.0e^{-7}$ was used for the simulations throughout this thesis.
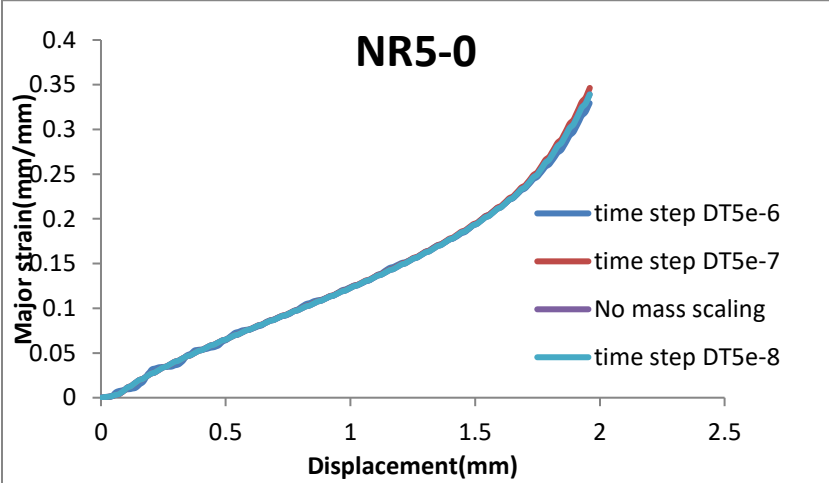
Figure3.5: Major strain for the first edge element in NR5-0 specimen versus displacement for different densities
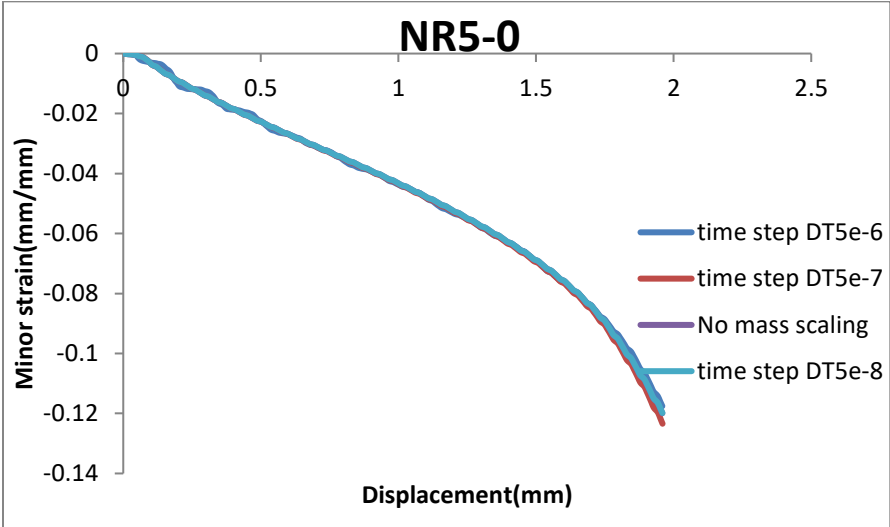
Figure3.6: Minor strain for the first edge element in NR5-0 specimen vs displacement for different densities

The location on the specimen that was used to extract the strain history from both experimental and numerical modeling results was adjusted for each specimen geometry. This was because the location of the element with the highest strain depended on the specimen geometry. For example, the highest strain in the NR5 specimen type was located near the outer edge at the smallest cross-sectional area of the specimen. Using DIC analysis, the major and minor strains in the four surface nodes surrounding this element were averaged and compared with those predicted by ABAQUS. From ABAQUS, logarithmic major and minor strains were extracted for the same surface element. For example, if the material orientation is longitudinal (0°) relative to the rolling direction, then LE11 would be the major strain and LE22 would be the minor strain. For the diagonal direction (45°), the major strain was the maximum principle logarithmic strain LEP33 and the minor strain was the minimum principle logarithmic strain LEP11. For the transverse direction(90°), the major and minor strains were LE11 and LE22, respectively. Directions "1" and "2" are as schematically shown in Figure 3.7.

| Longitudinal direction 0° | Transverse direction 90° | Diagonal direction 45° |
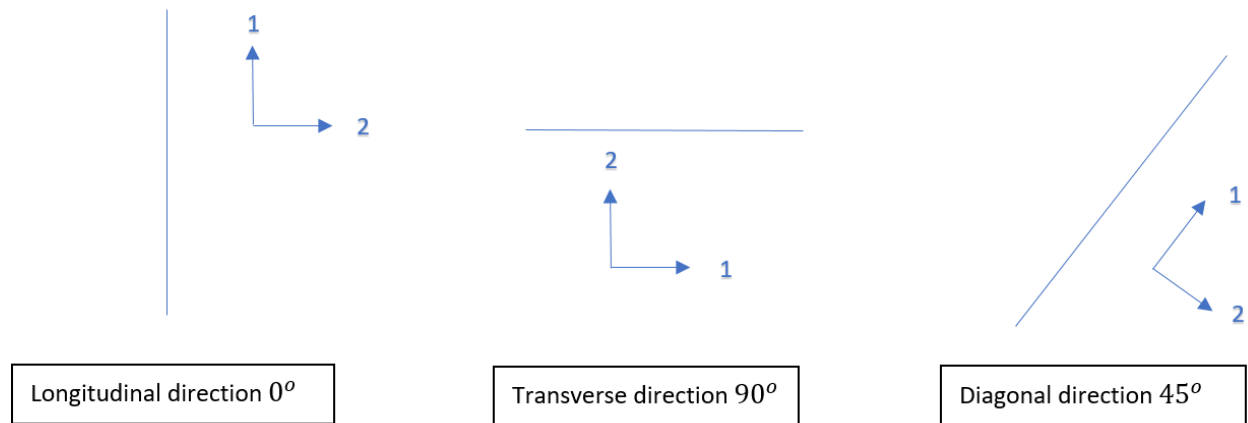
Figure3.7:Material orientations (LD, TD and DD) and the directions (1 and 2) used in ABAQUS

3.2.2 DIC-ABAQUS Strain Analyses

A study was performed on NR5-0 specimens (NR5 specimen with the major testing axis parallel to the rolling direction of the sheet) in order to understand the strain variation within the

width of the critical region and to identify the element to be used for comparison between DIC and ABAQUS. Values of the strain variation versus displacement for nodes numbered 0 to14 are shown in Figure 3.8. The highest major strain was found to be at node 0 (an edge node). The strain decreased in each node when moving from the edge toward the center of the specimen. Furthermore, the absolute values of the minor strains were shown to have the same trend (maximum at the edge, decreasing toward the center of the specimen).
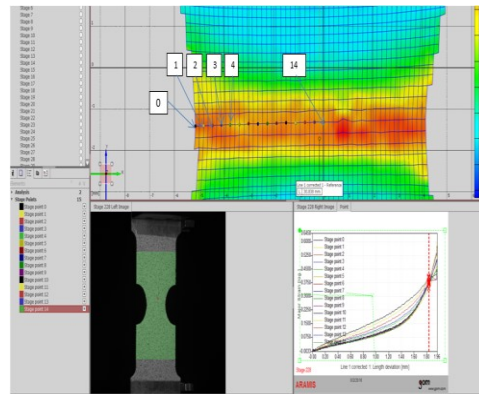
(a)
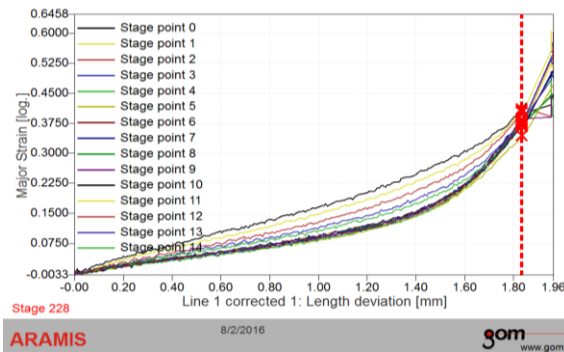
(b)
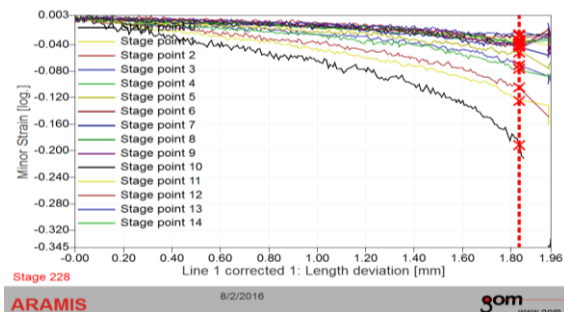
(c)

Figure3.8:(a) Nodes picked in the analyses of the NR5-0 specimen, (b) major and (c) minor strains versus gage displacement extracted from DIC for different nodes

Since the specimen was symmetric, the same comparison was performed on both sides (across the width) of the NR5-0 specimen. The analysis showed similar results for both sides. Thus, for the NR5-0 specimens, the first edge element on either the left side or right side may be used in the comparison with ABAQUS.

This same procedure was also conducted on a NR5-0 specimen in ABAQUS where the results showed that the first edge node had the highest major strain and that the center node had the lowest major strain.

The comparison for the major and minor strains between DIC and ABAQUS for NR5 specimens was made between the first edge element 415 as seen in Figure 3.9, and the four surface edge nodes in DIC. Table 3.4 summaries the location of the elements selected for the comparison between DIC and ABAQUS.

(a)　　　　　　　　　　　　　　　(b)
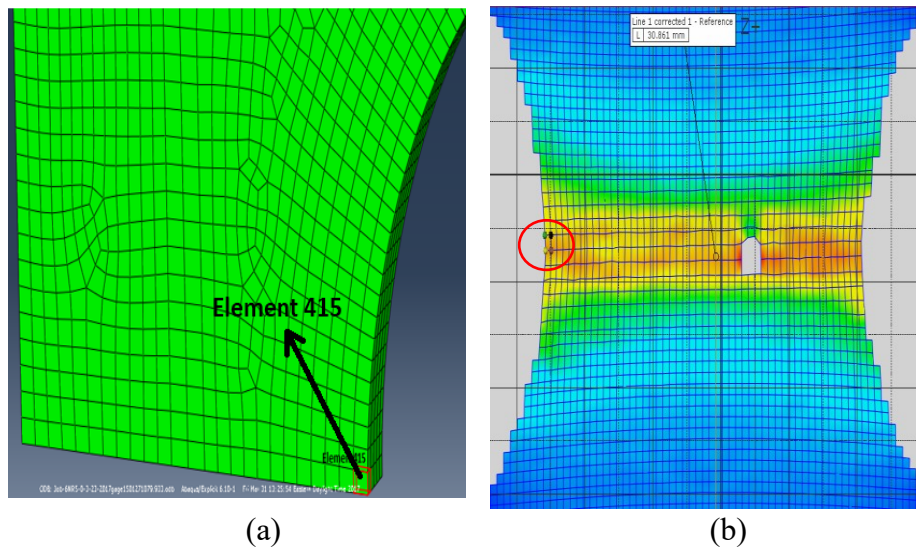
Figure3.9: Elements selected for the comparison of strains between (a) ABAQUS and (b) DIC

Table 3.4: Elements picked for comparison between DIC and ABAQUS for different specimen geometries

	DIC		ABAQUS	
	Fracture initiate	Highest strain	Highest strain	Most damage element picked
DB-0	Center	center	Center	Center
DB-45	Center	center	Center	Center
DB-90	Center	center	Center	Center
NR5-0	Edge	edge	Edge	Edge

NR5-45	Edge	edge	Edge	Edge
NR5-90	Edge	edge	Edge	Edge
NR10-0	Center	center	Center	Center
NR10-45	Center	center	Center	Center
NR10-90	Center	center	Center	Center
NR20-0	Center	center	Edge	Center
NR20-45	Center	center	Edge	Center
NR20-90	Center	center	Edge	Center
CH0	hole edge	hole edge	hole edge	hole edge
CH-45	hole edge	hole edge	hole edge	hole edge
CH-90	hole edge	hole edge	hole edge	hole edge

3.2.3 Simulation Results and comparison with the experiments

3.2.3.1 Uniaxial tensile tests

The first simulations (using ABAQUS) were performed on the uniaxial tension specimens to examine the model's ability to predict the evolution of strains. The selection of the elements used for the comparison between DIC and ABAQUS was based on the following:

- Visually examining the DIC results for the stage during which fracture initiated, then identifying the element with the highest strain in the gage section.
- If the element with the highest strain was not at the same location where the fracture initiated, the element located where the fracture initiated was chosen. For example, for the uniaxial tension specimens the selected element was in the center of the gage section.

Figure 3.10 presents the comparison between experimental data and the simulations. Overall, the simulation and the DIC results (experimental) followed the same evolution path for the RD (0°) direction (Figure 3.10 a), but for the DD (45°) and TD (90°) directions, the simulation predicted earlier strain localization., as can be seen in Figure 3.10b and c. The elastic, yielding and hardening behavior, onset of necking and the evolution of the major strain with displacement exhibited by the DB0 specimen is perfectly captured by the simulation. The simulations were able to capture the elastic, yielding and hardening behavior of the DB45 specimen. However, the model predicted an earlier occurrence of plastic instability as shown in Figure 3.10 b. Finally, the model showed a good prediction of the mechanical behavior of the DB90 specimen up to failure. However, a slight difference in the evolution of the major strains can be observed, and precisely around the maximum

load.
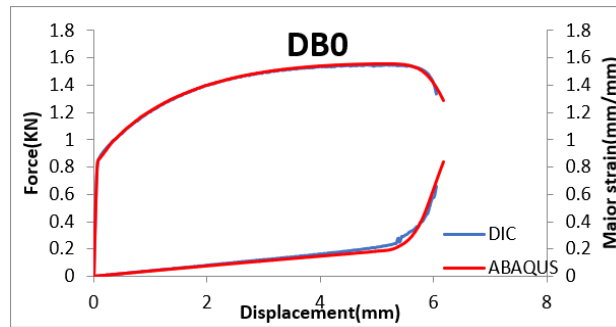
(a)
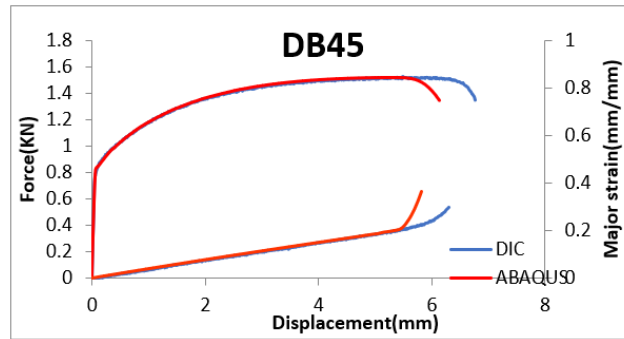
(b)
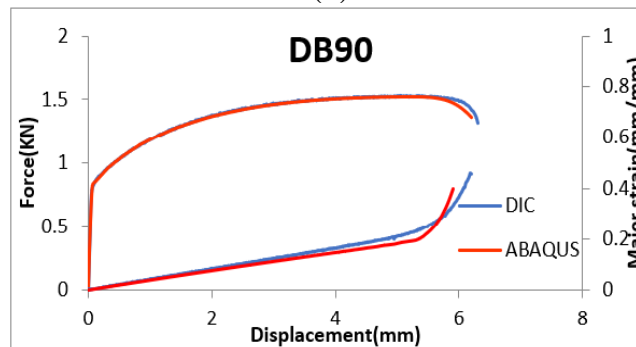
(c)

Figure3.10: Comparison between DIC and simulation of uniaxial tension specimens in a) 0⁰ b) 45⁰ c) 90⁰

3.2.3.2 Simulation of notch radius specimens

For NR5 specimens, the highest strain element was located at the edge. Therefore, the edge element was used in the comparison between DIC and ABAQUS. However, for NR10 and NR20 specimens, the highest strain element was found to be at the center of the gage section.

The simulation results for NR5 specimens loaded in the RD, DD and TD directions are shown in Figure 3.11. The results showed a good match between simulation and experiments for the RD and DD directions in terms of the force-displacement responses, including the post necking portion of the curve, as well as the true strain-displacement curve. However, for the TD direction, the DIC results showed an early necking behavior as can be seen in Figure 3.11 c.

The simulation results for NR10 specimens are shown in figure 3.12. A good match was obtained between the simulation and experimental results for the specimens loaded in the RD and DD directions. But also, an early necking was shown in the DIC results for the transverse direction specimens.

The simulation results for NR20 specimens are shown in figure 3.13. A mismatch at the necking phase between the DIC and the simulation results was shown in the specimens loaded in the DD direction, where the simulation predicted an early fracture.
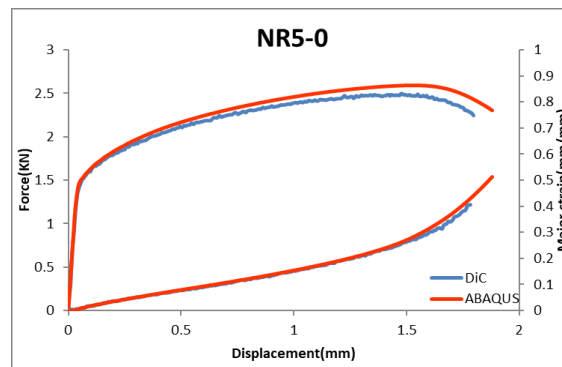
(a)
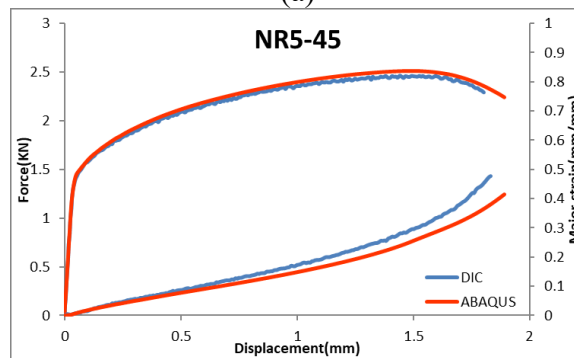
(b)
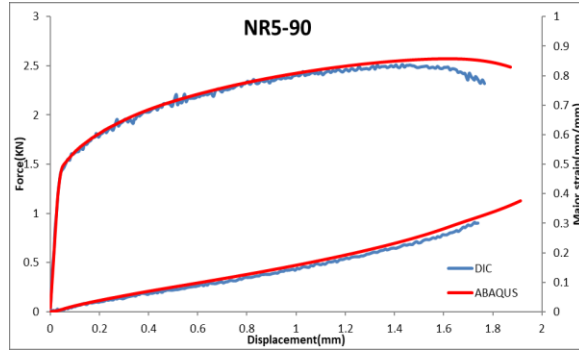
(c)

Figure3.11: Comparison of experimental and simulation results in both force versus displacement results and logarithmic strain versus displacement for notch radius 5 specimens in LD, DD and TD

(a)

(b)

(c)

Figure3.12:Comparison of experimental and simulation results in both force versus displacement results and logarithmic strain versus displacement for notch radius 10 specimens in LD, DD and TD

(a)

(b)

(c)

Figure3.13: Comparison of experimental and simulation results in both force versus displacement results and logarithmic strain versus displacement for notch radius20 specimens in LD, DD and TD

3.2.3.3 Simulation of central hole

The simulation results for central hole specimens tested in the three orientations RD, DD, and TD are shown in Figure 3.14. The result showed a good match between the simulation and experimental results, in both force-displacement responses, as well as the true strain-displacement curve up to necking. However, for all the three directions, the DIC results showed an early necking behavior that was clearly observable in the force-displacement curve. Although the model was unable to predict the force decrease at fracture, the model was able to predict the evolution of the major strain up to fracture for the three tested sheet orientations. The simulations could not predict the softening induced by fracture, only the onset of plastic instability, which theoretically would occur at much higher deformation.

(a)
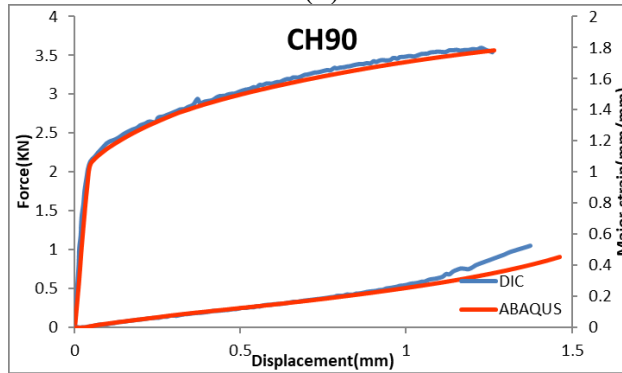
Figure3.14: Comparison of experimental and simulation results in both force versus displacement results and logarithmic strain versus displacement for central hole specimens in a) 0° b) 45⁰ c) 90⁰

3.2.3.4 Simulation of shear specimens

The comparison between the simulation and experimental results for the shear specimens tested in the three sheet directions TD, DD, and RD are shown in Figure 3.15. The results showed a shift between the simulation and the experimental results especially in the elastic region for the RD, DD and TD directions. The shift was observed in the force-displacement responses, as well as the true strain-displacement in DD, which might have been caused by anisotropic hardening. In the simulations, an isotropic elastic stiffness tensor, was used with a young modulus E = 69 GPa and the Poisson's ratio μ = 0.3. The difference between the experimental results and the simulations might be reduced by using an anisotropic stiffness tensor (cubic symmetry stiffness tensor), but this was not attempted in this study.
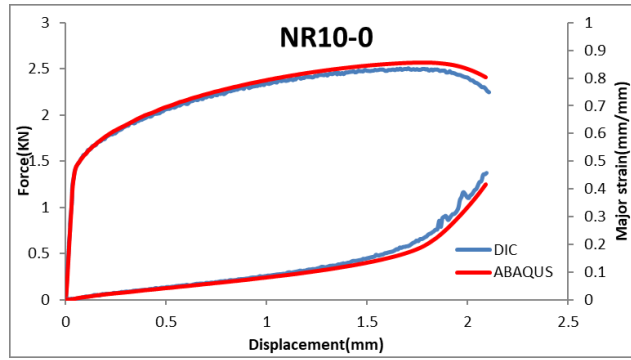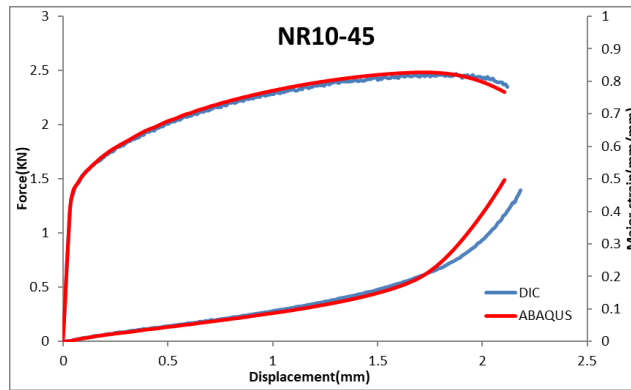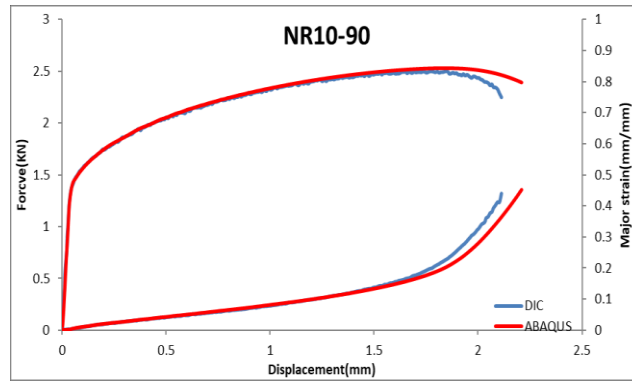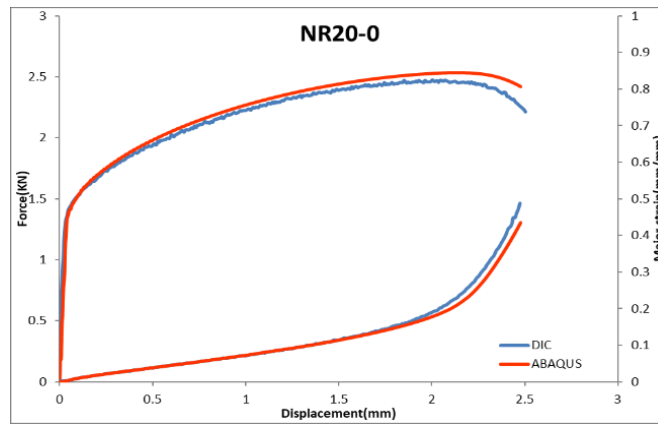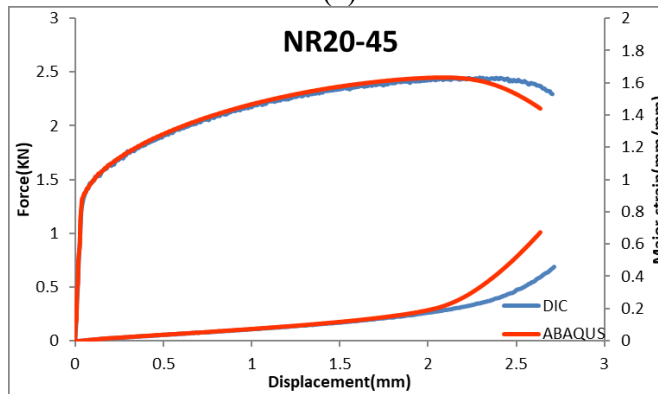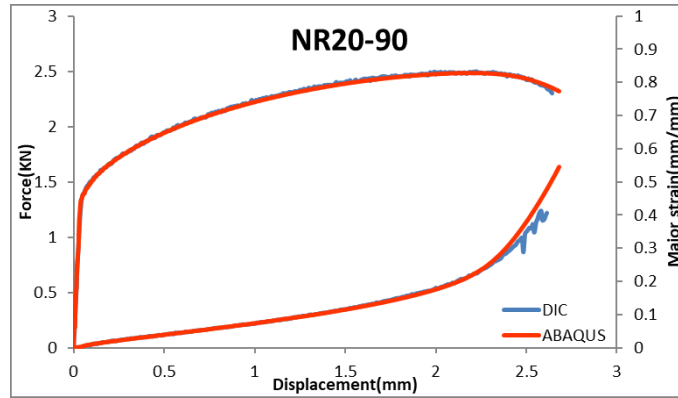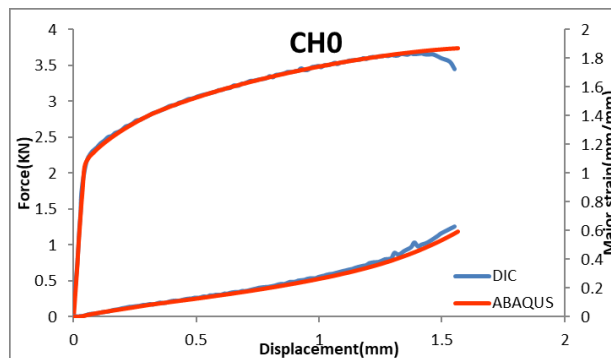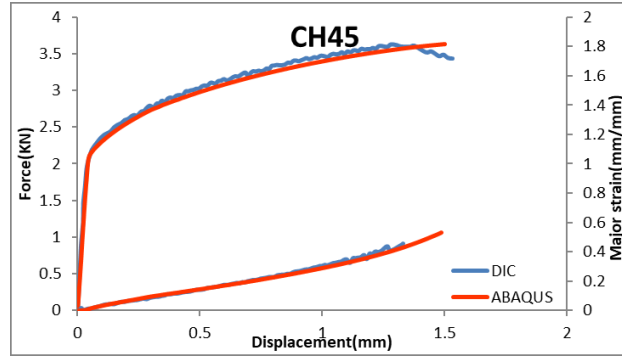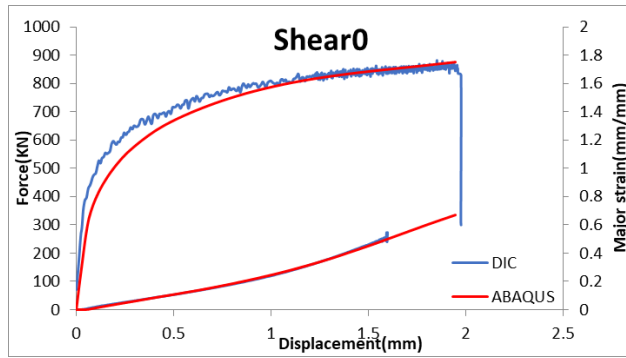
(a)
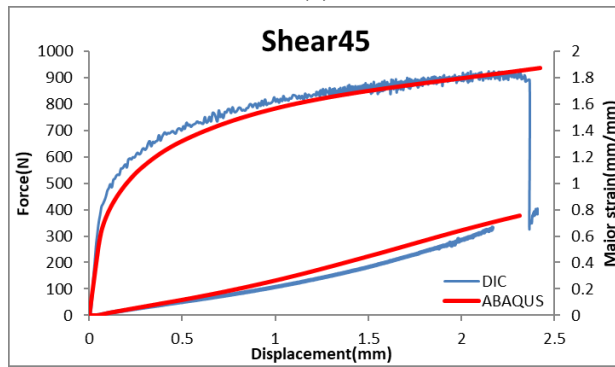
(b)
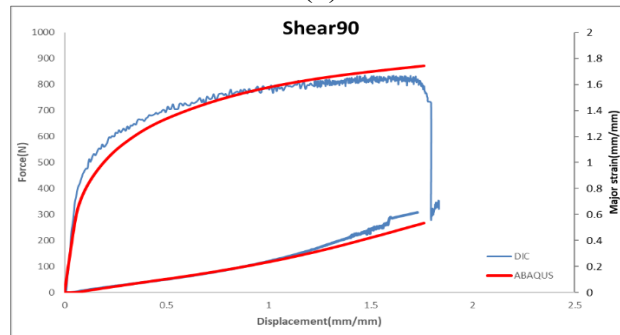
(c)

Figure3.15: Comparison of experimental and simulation results in both force versus displacement results and logarithmic strain versus displacement for shear specimens in a) 0º b) 45⁰ c) 90⁰

3.2.4 Triaxiality and Lode Angle Variation

49
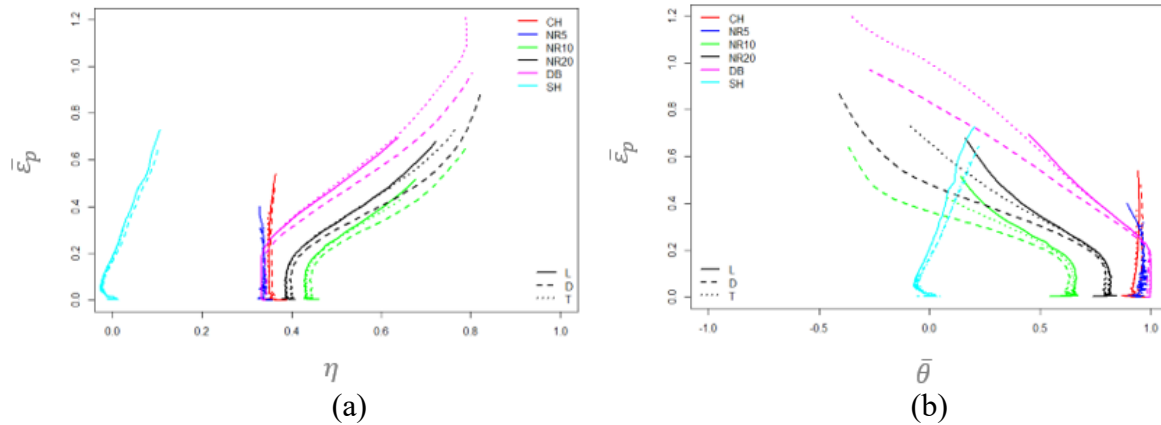
Figure3.16: Variation of the effective plastic strain versus (a) triaxiality and (b) lode angle, for the different tested specimens and at different material orientations

Figure 3.16 presents the evolution of the normalized lode angle θ and the triaxiality η as functions of the equivalent plastic strain, extracted from the simulations of the CH, NR5, NR10, NR20, DB and SH specimens. The following observations were made:

- The stress state developed in the shear specimens was close to pure shear as the triaxiality and lode angle were almost zero.
- For the CH and the NR5 specimens, the triaxiality and lode angle were almost the same. The triaxiality value was equal to 0.33, which indicated that the stress state in both specimens was uniaxial tension up to the fracture initiation.
- For the DB specimen, the deformation started as uniaxial tension as the values of the equivalent strain to fracture versus triaxiality or lode angle were very similar to those of the CH and NR5 specimens. At an equivalent plastic strain of 0.23, the triaxiality increased and the lode angle decreased, which was indicative of the evolution of the stress state from uniaxial to plane strain.
- For the NR10 and the NR20 specimens, the stress state was close to uniaxial tension at the beginning of the deformation. At an equivalent plastic strain of 0.2 the stress triaxiality increased and the lode angle decreased, resulting into a progressive evolution of the stress state to plane strain.

50

Chapter 4: Fracture Surface Identifications

In this chapter, two fracture surface models were investigated, the modified Mohr Coulomb (MMC) model and the Hosford Coulomb (HC) model. Two types of calibration procedures were used: (a) a hybrid method and (b) a direct method. In the hybrid calibration method as shown in figure 4.1, a damage accumulation rule was used which is based on an incremental relation between the equivalent plastic strain and a damage indicator as follow:

$$D = \int_0^{\bar{\varepsilon}_p} \frac{d\bar{\varepsilon}_p}{\bar{\varepsilon}_f\left[\eta,\bar{\theta}\right]} \tag{4.1}$$

This function has an initial value of zero and it starts accumulating damage at the onset of plastic deformation and considers fracture to initiate when D reaches a value of 1.0. In addition, the hybrid calibration requires simulation results (lode angle and triaxiality evolution) for the fractured tests to calculate the damage evolution up to the fracture stage. The specimens used for the calibration are NR5, NR10, NR20, CH, SH in the three material orientations (RD, DD and TD). The tests used for the verification of the model prediction capabilities are Marciniak, Hole expansion, Shear and Mini-punch.
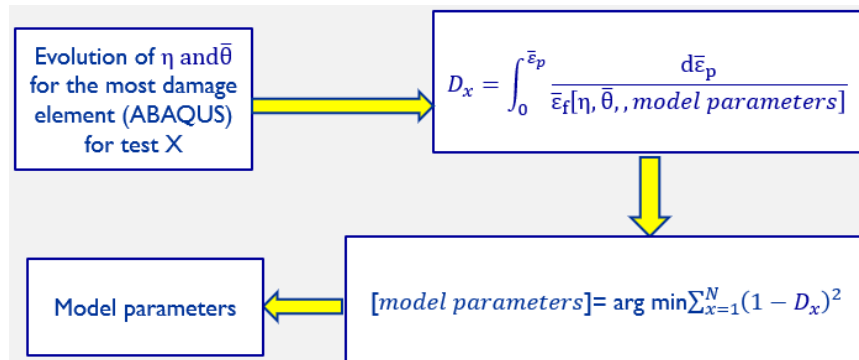
Figure 4.1: Schematic of the hybrid calibration process

The direct calibration method requires only experimental results. The experimental results used in the method presents a constant triaxiality and lode angle all the way to fracture. The direct calibration of the fracture surfaces is proceeded using Mini-punch, Marciniak, Hole expansion, Shear while NR5, NR10, NR20, CH, SH tests are used to model fracture prediction capability. A schematic of the direct calibration process is shown in figure 4.2.
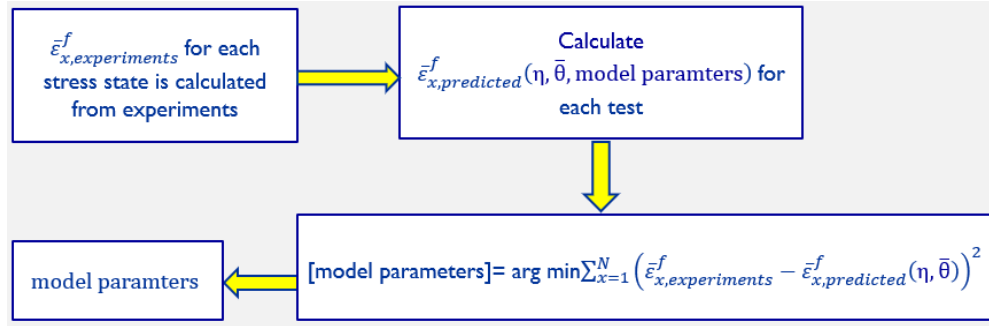
Figure 4. 2: Schematic of the direct calibration process

4.1 Modified Mohr Coulomb (MMC) Theoretical background

The MMC fracture criteria, developed by Bai & Wierzbicki (2010), was used to describe the fracture of Al-6DR1 ductile material by transforming the stress based Mohr-Coulomb fracture criteria into the base of equivalent plastic strain, lode parameter and stress triaxiality. The Mohr-Coulomb fracture criteria was proven to predict the following:

- The exponential decay of the material ductility
- The orientation of the fracture surface
- The form of lode angle dependence (close to parabolic)

The mathematical formulation for this criterion was reported by Bai & Wierzbicki (2010) and is shown in equations 4.2 through 4.11.

The stress tensor has three invariants defined as P, Q and R:

$$P = -\sigma_m = -\frac{1}{3}\left(\sigma_I + \sigma_{II} + \sigma_{III}\right) \qquad\qquad \textbf{4. 2}$$

$$Q = \bar{\sigma} = \sqrt{\frac{1}{2}\left[\left(\sigma_I - \sigma_{II}\right)^2 + \left(\sigma_{II} - \sigma_{III}\right)^2 + \left(\sigma_{III} - \sigma_I\right)^2\right]} \qquad\qquad \textbf{4. 3}$$

$$R = \left[\frac{27}{2} \left(\sigma_I - \sigma_m \right) \left(\sigma_{II} - \sigma_m \right) \left(\sigma_{III} - \sigma_m \right) \right]^{1/3}$$ **4. 4**

The stress triaxiality is the hydrostatic pressure normalized over the von Mises stress:

$$\eta = \frac{-P}{Q} = \frac{\sigma_m}{\bar{\sigma}}$$ **4. 5**

Normalized third invariant

$$\xi = \left(\frac{R}{Q} \right)^3 = \cos(3\theta)$$ **4. 6**

Where, $-1 \leq \xi \leq 1$, and θ is the Lode angle ($0 \leq \theta \leq \frac{\pi}{3}$)

Normalized Lode angle

$$\bar{\theta} = 1 - \frac{6\theta}{\pi} = 1 - \frac{2}{\pi} \arccos \xi$$ **4. 7**

where $-1 \leq \bar{\theta} \leq 1$

According to the Mohr-Coulomb (M-C) fracture criteria, fracture occurs when the normal and shear stress reaches a critical value:

$$\left(\tau + c_1 \sigma_n \right) = c_2$$ **4. 8**

where c_1 is a friction coefficient, and c_2 is a shear resistance.

The M-C criterion expressed in terms of the von Mises stress at fracture initiation ($\bar{\sigma}$), θ and η takes the form:

$$\bar{\sigma} = c_2 \left[\sqrt{\frac{1+c_1^2}{3}} \cos\left(\frac{\bar{\theta}\pi}{6} \right) + c_1 \left(\eta + \frac{1}{3} \sin\left(\frac{\bar{\theta}\pi}{6} \right) \right) \right]^{-1}$$ **4. 9**

The M-C criteria was extended to a strain based to increase the resolution of the ductile fracture prediction using a generalized hardening law with pressure and lode angle dependence.

$$\bar{\sigma} = A\bar{\varepsilon}_f \left[c_3 + \frac{\sqrt{3}}{2-\sqrt{3}} (1-c_3) \left(\sec\left(\frac{\bar{\theta}\pi}{6} \right) - 1 \right) \right]$$ **4. 10**

where A is a material constant, n is a strain hardening component and by adjusting the parameter

c_3 various shapes of the yield surface can be obtained.

The strain-based MMC criteria is as follows:

$$\bar{\varepsilon}_f = \left\{ \frac{A}{c_2} \left(c_3 + \frac{\sqrt{3}}{2-\sqrt{3}}(1-c_3) \left(\sec\left(\frac{\bar{\theta}\pi}{6}\right) - 1 \right) \right) \left(\sqrt{\frac{1+C_1^2}{3}} \cos\left(\frac{\bar{\theta}\pi}{6}\right) + C_1 \left(\eta + \frac{1}{3}\sin\left(\frac{\bar{\theta}\pi}{6}\right) \right) \right) \right\}^{-\frac{1}{n}} \qquad \textbf{4. 11}$$

where A, n are parameters of material strain hardening. C_1, C_2, C_3 are the fracture model parameters that needs to be determined from calibration and η, $\bar{\theta}$ are the lode angle and stress triaxiality respectively.

Aluminum sheets are challenging to model since they exhibit an anisotropic response in their plastic and fracture behaviors. To provide a wide range of stress states, several types of experiments are conducted. To account for the effect of anisotropy at fracture, three different orientations (0^0, 45^0, 90^0) are considered. The different types of specimens used to build the fracture surface are shown in Table 4.1. Specimens were tested using a servo-hydraulic testing machine (MTS Model 204.52) at a constant crosshead velocity of 0.5mm/min. The load and crosshead displacement were recorded during each test. In addition, a digital image correlation (DIC) equipment was used to capture the surface strain distribution. The DIC software ARAMIS v6.3.0 was used for the DIC analysis. To verify the repeatability of the tests, at least three specimens were tested for each experimental condition.

Table 4.1: stress state for different specimen geometries

Specimen type	Stress state (at gage section)
Notch radius 5-10-20 mm	As R increases, the stress state change from plane strain to uniaxial tension next to the sample center.
Uniaxial tension	Stress state changes from uniaxial tension to transverse plane strain due to necking.
Central hole (alternative to DB)	Stress state stays uniaxial tension up to fracture initiation.
Shear	Stress state is simple shear.
Equi-biaxial tension	Stress state is biaxial in the center of the sample

4.1.1 MMC model fracture surface results

The calibrated model parameters for the MMC model are shown in table 4.2. The identified model parameters and the evolution of η and $\bar{\theta}$ with displacement up to the point of experimental fracture extracted from the Abaqus simulations is used as input for calculating the damage indicator D. Theoretically, fracture is assumed to occur when D reaches 1. The damage indicator is calculated up to the point of experimental fracture. Therefore, if the calculated damage indicator is equal to one at the point of experimental fracture then the model capability to predict fracture is validated. Figure 4.1 presents the values of the damage indicator calculated up to the point of experimental fracture for the different specimens used in this study.

The model predictions with the hybrid calibration method are conservative for DB-0, DB-45, DB-90, NR10-45, NR20-0, NR20-45, NR20-90, SH-0, PST, UT, EBT. In addition, the model predicts a delayed fracture for CH-0, CH-45, CH-90, NR10-0, NR10-90, NR5-0, NR5-45, NR5-90. The model is able to predict with a small error the experimental fracture for SH45, SH90.

Furthermore, the model predictions with the direct calibration method are conservative for DB45, DB90, NR20-45. However, the model predicts a delayed fracture, for CH-0, CH-45, CH-90, DB-0, NR10-0, NR10-45, NR10-90, NR20-0, NR20-90, NR5-0, NR5-45, NR5-90, SH-45, SH-90. The model can predict the experimental results with a small error for SH0, PST, UT, EBT.

Table 4.2: MMC model parameters

Calibration Method	C_1	C_2	C_3
Hybrid	0.007825032	170.4063	0.8660254
Direct	0.001	181.4327	0.8923009

(a)   (b)
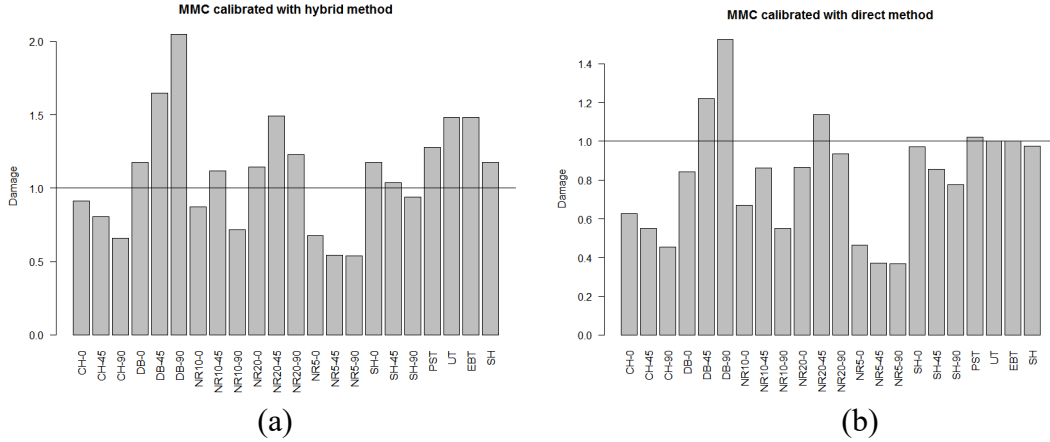
Figure 4.3: Damage evolution for the different tested specimen using an MMC model calibrated with (a) a hybrid method and (b) a direct method

4.2 Hosford-Coulomb (H-C) Model, Theoretical Background

In Mohr and Marcadet, 2015 the onset of localization prediction was based on a non-porous plasticity model coupled with a localization criterion. The authors modified the M-C model to improve the prediction of the onset of fracture by replacing the Tresca equivalent stress with the Hosford equivalent stress. Furthermore, a damage indicator is proposed to account for non-proportional loading. Their results showed that their proposed model provided good fracture predictions for a variety of materials. The mathematical framework of the proposed Hosford-Coulomb (HC) model is summarized here:

The MC model defined in Eq. (4.8) can be re-written as follows:

$$\left(\sigma_{I} - \sigma_{III}\right) + c\left(\sigma_{I} + \sigma_{III}\right) = \beta \qquad \textbf{4. 12}$$

Where, σ_{I} and σ_{III} are the principal stresses, c and β are material constants. The Eq. (4.12) can be re-written to define the HC criterion as follows:

$$g_{HC}\left[\boldsymbol{\sigma}\right] = \bar{\sigma}_{HF} + c\left(\boldsymbol{\sigma}_{I} + \boldsymbol{\sigma}_{III}\right) = \beta \qquad \textbf{4. 13}$$

where the Hosford equivalent stress is defined as

$$\bar{\sigma}_{HF} = \left\{ \frac{1}{2} \left(\left(\sigma_I - \sigma_{II} \right)^a + \left(\sigma_{II} - \sigma_{III} \right)^a + \left(\sigma_I - \sigma_{III} \right)^a \right) \right\}^{\frac{1}{a}}$$

       4. 14

With a denoting the Hosford exponent. The state of anisotropy is described using a Cauchy stress tensor normalized by Von Mises equivalent stress. The yield function used is Barlat YLD2000-3D, the description of its theoretical formulation is already shown in chapter 3.

An associated plastic flow rule was assumed as shown below:

$$d\varepsilon_p = d\lambda \frac{\partial f}{\partial \sigma}$$

       4. 15

where $d\varepsilon_p$ represent a plastic strain tensor and $d\lambda$ is a scalar plastic multiplier.

$$d\varepsilon_p = \bar{\sigma}_a d\bar{\varepsilon}_a \text{ , where } \bar{\varepsilon}_a \text{ is the anisotropic equivalent plastic strain } \bar{\varepsilon}_a = \int d\lambda$$

       4. 16

A Swift-Voce law is used to describe the isotropic hardening behavior:

$$k\left[\bar{\varepsilon}_a \right] = wA_s \left(\varepsilon_0 + \bar{\varepsilon}_a \right)^{n_s} + (1-w) \left\{ k_0 + Q \left(1 - e^{-\beta \bar{\varepsilon}_p} \right) \right\} \text{ where w is a weighting factor,}$$

$\{A_s, \varepsilon_0 n_s, k_0, Q, \beta\}$ are Swift and Voce parameters.

       4. 17

The isotropic Hosford-Coulomb in function of stress triaxiality and lode angle is as follow

$$g_{HC} = \left[\eta, \bar{\theta} \right] = \left\{ \frac{1}{2} \left(\left(f_1 - f_2 \right)^a + \left(f_2 - f_3 \right)^a + \left(f_1 - f_3 \right)^a \right) \right\}^{\frac{1}{a}} + c \left(2\eta + f_1 + f_3 \right)$$

       4. 18

$$\left[\bar{\theta} \right] = 1 - \frac{2}{\pi} \arccos \left[-\frac{27}{2} \eta \left(\eta^2 - \frac{1}{3} \right) \right] \text{ for } -\frac{2}{3} \leq \eta \leq \frac{2}{3}$$

       4. 19

$$f_1 \left[\bar{\theta} \right] = \frac{2}{3} \cos \left[\frac{\pi}{6} \left(1 - \bar{\theta} \right) \right]$$

       4. 20

$$f_2 \left[\bar{\theta} \right] = \frac{2}{3} \cos \left[\frac{\pi}{6} \left(3 + \bar{\theta} \right) \right]$$

       4. 21

$$f_3 \left[\bar{\theta} \right] = -\frac{2}{3} \cos \left[\frac{\pi}{6} \left(1 + \bar{\theta} \right) \right]$$

       4. 22

In this model, the fracture strain for equi-biaxial tension and uniaxial tension are considered to be equivalent due to the maximum principle stress and the Hosford equivalent stress being equal.

Roth and Mohr (2016) proposed an experimental calculation of the stress to fracture under proportional loading using the following four experiments: uniaxial tension, equi-biaxial tension, plane strain tension and shear. They used an H-C model to predict fracture, which included an isotropic yield function and a Swift-Voce combination to predict the hardening behavior. As discussed in Mohr and Marcadet (2015), the H-C fracture criterion is transformed into the mixed stress strain space using the relationship described by equation (4.17)

$$\bar{\varepsilon}_f^{pr}\left[\eta,\bar{\theta}\right] = b\left(1+c\right)^{\frac{1}{n}}\left(\left\{\frac{1}{2}\left(\left(f_1 - f_2\right)^a + \left(f_2 - f_3\right)^a + \left(f_1 - f_3\right)^a\right)\right\}^{\frac{1}{a}} + c\left(2\eta + f_1 + f_3\right)\right)^{-\frac{1}{n}} \qquad \textbf{4. 23}$$

with n=0.1 and (a, b, c) are the model parameters.

The strain to fracture was characterized experimentally as shown in table4.3.

Table 4.3: Strain to fracture, triaxiality and lode angle for different stress states

STRESS STATE	STRAIN TO FRACTURE	TRIAXIALITY	LODE ANGLE
Pure shear	$\bar{\varepsilon}_f^{SH} = b\left(\sqrt{3}\,\dfrac{1+c}{(1+2^{a-1})^{\frac{1}{a}}}\right)^{\frac{1}{n}}$	0	0
Uniaxial tension	$\bar{\varepsilon}_f^{UT} = b$	0.333	1
Plane strain tension	$\bar{\varepsilon}_f^{PST} = b\left(\sqrt{3}\,\dfrac{1+c}{(1+2^{a-1})^{\frac{1}{a}}+2c}\right)^{\frac{1}{n}}$	0.577	0
Equi-biaxial tension	$\bar{\varepsilon}_f^{EBT} = b$	0.666	-1

The model parameter *b* was determined from uniaxial tension or equi-biaxial tension, and the parameters *c* and *a* were determined from equations (4.24) and (4.25):

$$c = \frac{1 - \left(\dfrac{\overline{\varepsilon}_f^{PST}}{\overline{\varepsilon}_f^{SH}}\right)^n}{\dfrac{2}{\sqrt{3}}\left(\dfrac{\overline{\varepsilon}_f^{PST}}{b}\right)^n + \left(\dfrac{\overline{\varepsilon}_f^{PST}}{\overline{\varepsilon}_f^{SH}}\right)^n - 1} \qquad\qquad \textbf{4. 24}$$

$$\left(1 + 2^{a-1}\right)^{\frac{1}{a}} = \sqrt{3}\left(1 + c\right)\left(\dfrac{b}{\overline{\varepsilon}_f^{SH}}\right)^n , \; 1 \le a \le 2 \qquad\qquad \textbf{4. 25}$$

The suggested experiments have the advantage of constant stress state up to the point of fracture initiation. which greatly simplifies model calibration. The limitations of this model are the following:

- Plane strain cannot be obtained from the 3 point-bending test for ductile materials or thin sheets (i.e. AL6DR1.)
- The process is not purely experimental because the uniaxial tension specimen (CH) requires simulation to get the strain in the most damage element in the thickness.

In this work, an attempt was made to build a purely experimental fracture surface for proportional loading. Two alternative tests were proposed to identify the local strain at onset of fracture under plane strain and uniaxial strain, namely, the Marciniak test and the hole-expansion test, respectively.

4.2.1 HC model fracture surface results

To generate the fracture surface, the equivalent plastic strain at onset of fracture under pure shear (45° direction), plane strain (Marciniak test), balanced biaxial (mini punch test), and uniaxial (hole expansion test) testing conditions were used. The fracture strains for these four experiments performed under proportional loading are shown in Tables 4.4. It is worth mentioning that the SH45 is used as the principal directions are along the TD and RD directions.

Table 4.4: Equivalent plastic strain used for the fracture surface calculation

	Major strain	Equivalent plastic strain
Shear test 45°	0.69	0.73
Marciniak test (TD and RD)	0.66	0.76
Mini punch test	0.46	0.86
Hole expansion test	0.78	0.78

The Hosford-Coulomb parameters a, b and c are calculated from the experimental measurements of the strain to fracture using table 4.3 and equations (4.29) and (4.30). Once these parameters are calculated, equation (4.27) is used to determine the fracture surface.

(a)   (b)
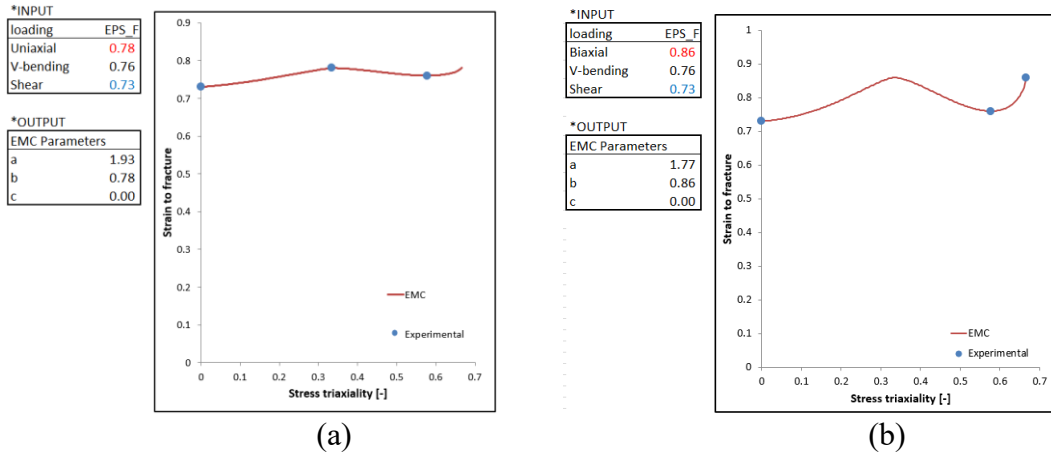
Figure 4.4: Strain to fracture versus triaxiality using (a) the uniaxial results and (b) the biaxial results

The calibrated HC fracture model parameters are shown in table 4.6. The values of the damage indicator calculated up to the point of experimental fracture are shown in Figure 4.1.

With hybrid calibration method, the model predicts an early fracture (conservative prediction), for DB-0, DB-45, DB-90, NR10-45, NR20-0, NR20-45, NR20-90, SH-0, PST, UT, EBT. In addition, the model predicts a delayed fracture for CH-0, CH-45, CH-90, NR10-0, NR10-90, NR5-0, NR5-45, NR5-90.

Furthermore, the model predictions are comparable to experimental fracture results for the SH-0, PST, UT, EBT and SH. However, the model predicts an early fracture (conservative prediction), for DB45, DB90, NR20-45. In addition, the model predicts a delayed fracture for CH-0, CH-45, CH-90, DB-0, NR10-0, NR10-45, NR10-90, NR20-0, NR20-90, NR5-0, NR5-45, NR5-90, SH-45, SH-90.

Table 4.5: HC model calibration parameters

Calibration Method	a	b	C
Hybrid	2	0.5988352	0
Direct	1.720849	0.8800006	0

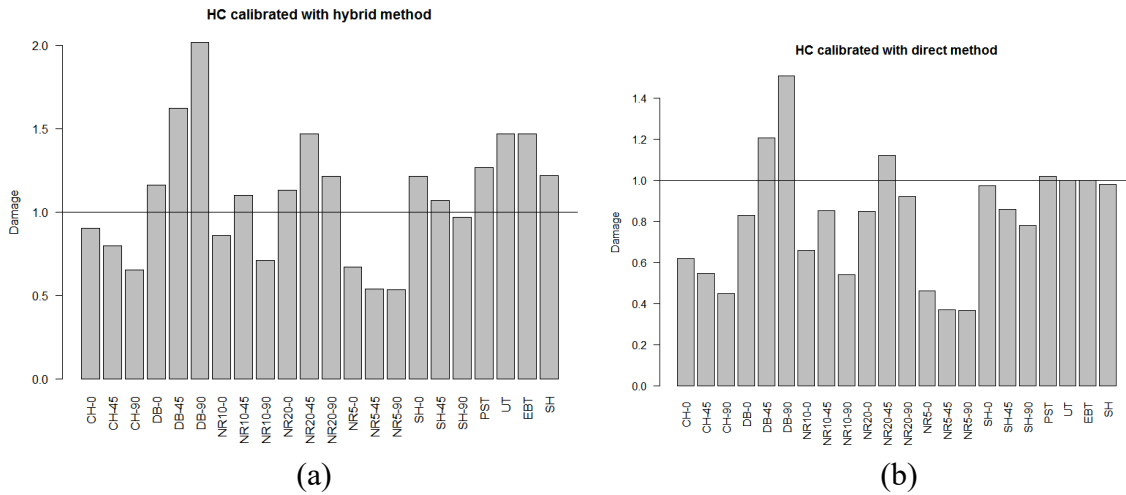(a)   (b)

Figure 4.5: Damage evolution for the different tested specimens using an HC model calibrated with a (a) hybrid method and (b) direct method

Chapter 5: Conclusion

The anisotropic ductile fracture behavior of 1 mm thick AL-6DR1 aluminum sheets is investigated. Two fracture models (MMC and HC) were used to predict the ductile behavior of the material. A series of test were conducted to cover a wide range of stress state for proportional loading conditions (Marciniak, Mini-punch, CH, Shear, Hole expansion) and for non-proportional loading conditions (NR5, NR10, NR20) at different sheet surface orientations (RD, DD, TD). The local and global strains evolution developed by the different studied specimens were measured using Digital Image Correlation (DIC) analysis method. The anisotropic behavior of the material was captured using a material subroutine, the yielding is described with YLD-2000-3D model and the plastic behavior is described using an associated flow rule combined with isotropic and hardening. The evolution of local stresses and strains up to the fracture initiation were determined using finite element simulation. Two calibration methods were used for the fracture models: a hybrid and a direct method. The major conclusions drawn from this study are:

- The mean squared errors (MSE) of the MMC and HC fracture models are equal for the same calibration method as can be seen in figure 5.1.
- Calibrating the models using a hybrid method (MSE=0.15) lead to a higher mean squared error then the direct calibration method (MSE= 0.11).
- The MMC and HC fracture models are almost predicting the same fracture response (figure 5.2) which for some specimens under-predict and for others overpredict the experimental fracture behavior.
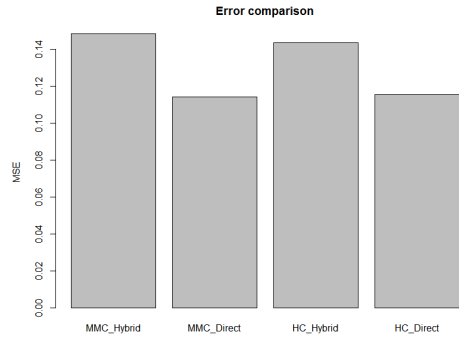
Figure 5.1: Mean squared error comparison for the MMC and HC models calibrated using both the hybrid and the direct methods
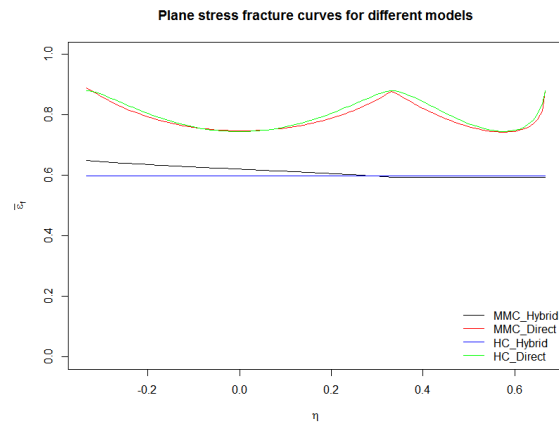

Figure 5.2: Plane stress representation of the different calibrated fracture models

References

Agarwal, H., Gokhale, A. M., Graham, S., & Horstemeyer, M. F. (2003). Void growth in 6061-aluminum alloy under triaxial stress state. *Materials Science and Engineering A*, *341*(1–2), 35–42. https://doi.org/10.1016/S0921-5093(02)00073-4

Bai, Y., & Wierzbicki, T. (2008). A new model of metal plasticity and fracture with pressure and Lode dependence. *International Journal of Plasticity*, *24*(6), 1071–1096. https://doi.org/10.1016/j.ijplas.2007.09.004

Bai, Y., & Wierzbicki, T. (2010). Application of extended Mohr-Coulomb criterion to ductile fracture. *International Journal of Fracture*, *161*(1), 1–20. https://doi.org/10.1007/s10704-009-9422-8

Barlat, F., Brem, J. C., Yoon, J. W., Chung, K., Dick, R. E., Lege, D. J., … Chu, E. (2003). Plane stress yield function for aluminum alloy sheets—part 1: theory. *International Journal of Plasticity*, *19*(9), 1297–1319. https://doi.org/http://dx.doi.org/10.1016/S0749-6419(02)00019-0

Barsoum, I., & Faleskog, J. (2011). Micromechanical analysis on the influence of the Lode parameter on void growth and coalescence. *International Journal of Solids and Structures*, *48*(6), 925–938. https://doi.org/10.1016/j.ijsolstr.2010.11.028

Benzerga, A. A. (2002). Micromechanics of coalescence in ductile fracture, *50*, 1331–1362.

Bong, H. J., Barlat, F., Lee, M. G., & Ahn, D. C. (2012). The forming limit diagram of ferritic stainless steel sheets: Experiments and modeling. *International Journal of Mechanical Sciences*, *64*(1), 1–10. https://doi.org/10.1016/j.ijmecsci.2012.08.009

Dorbane, A., Ayoub, G., Mansoor, B., Hamade, R., Kridli, G., & Imad, A. (2015). Observations of the mechanical response and evolution of damage of AA 6061-T6 under different strain rates and temperatures. *Materials Science and Engineering A*, *624*, 239–249. https://doi.org/10.1016/j.msea.2014.11.074

Dunand, M., Maertens, A. P., Luo, M., & Mohr, D. (2012a). Experiments and modeling of anisotropic aluminum extrusions under multi-axial loading - Part I: Plasticity. *International Journal of Plasticity*, *36*, 34–49. https://doi.org/10.1016/j.ijplas.2012.03.003

Dunand, M., Maertens, A. P., Luo, M., & Mohr, D. (2012b). Experiments and modeling of anisotropic aluminum extrusions under multi-axial loading - Part I: Plasticity. *International Journal of Plasticity*, *36*, 34–49. https://doi.org/10.1016/j.ijplas.2012.03.003

Gu, G., & Mohr, D. (2015). Anisotropic Hosford-Coulomb fracture initiation model: Theory and application. *Engineering Fracture Mechanics*, *147*, 480–497. https://doi.org/10.1016/j.engfracmech.2015.08.004

Gurson, A. L. (1977). Continuum Theory of Ductile Rupture by Void Nucleation and Growth: Part I—Yield Criteria and Flow Rules for Porous Ductile Media. *Journal of Engineering Materials and Technology*, *99*(1), 2. https://doi.org/10.1115/1.3443401

Hirsch, J. (2014). Recent development in aluminium for automotive applications. *Transactions of Nonferrous Metals Society of China (English Edition)*, *24*(7), 1995–2002.

https://doi.org/10.1016/S1003-6326(14)63305-7

Miller, W. S., Zhuang, L., Bottema, J., Wittebrood, A. J., De Smet, P., Haszler, A., & Vieregge, A. (2000). Recent development in aluminium alloys for the automotive industry. *Materials Science and Engineering A*, *280*(1), 37–49. https://doi.org/10.1016/S0921-5093(99)00653-X

Mohr, D., & Marcadet, S. J. (2015). Micromechanically-motivated phenomenological Hosford-Coulomb model for predicting ductile fracture initiation at low stress triaxialities. *International Journal of Solids and Structures*, *67–68*, 40–55. https://doi.org/10.1016/j.ijsolstr.2015.02.024

Needleman, A. & Tvergaard, V. (1984). An analysis of ductile rupture. *J Mech Phys Solids*, *32*(6), 461–490.

Pogatscher, S., Antrekowitsch, H., & Uggowitzer, P. J. (2012). Interdependent effect of chemical composition and thermal history on artificial aging of AA6061. *Acta Materialia*, *60*(15), 5545–5554. https://doi.org/10.1016/j.actamat.2012.06.061

Rice, J. R., & Tracey, D. M. (1969). On the ductile enlargement of voids in triaxial stress fields∗. *Journal of the Mechanics and Physics of Solids*, *17*(3), 201–217. https://doi.org/10.1016/0022-5096(69)90033-7

Roth, C. C., & Mohr, D. (2016). Ductile fracture experiments with locally proportional loading histories. *International Journal of Plasticity*, *79*, 328–354. https://doi.org/10.1016/j.ijplas.2015.08.004

Wierzbicki, T., Bao, Y., Lee, Y. W., & Bai, Y. (2005). Calibration and evaluation of seven fracture models. *International Journal of Mechanical Sciences*, *47*(4–5 SPEC. ISS.), 719–743. https://doi.org/10.1016/j.ijmecsci.2005.03.003

Zhang, K. (2001). Numerical analysis of the influence of the Lode parameter on void growth. *International Journal of Solids and Structures*, *38*(32–33), 5847–5856. https://doi.org/10.1016/S0020-7683(00)00391-7

Zhong, H., Rometsch, P., & Estrin, Y. (2014). Effect of alloy composition and heat treatment on mechanical performance of 6xxx aluminum alloys. *Transactions of Nonferrous Metals Society of China*, *24*(7), 2174–2178. https://doi.org/10.1016/S1003-6326(14)63329-X

Lemaitre, J. A (1992)*Course Of Damage Mechanics*. Paris: Library of congress cataloging in publication data.

Appendix

1. Basic of Strain in DIC

In DIC, all the measurements of strains, displacements and forces are done on the surface of the tested specimens. Strain is defined as the measure of deformation of an element. The following three types of strains can be measured in DIC:

- Technical strain: $\quad\quad\quad\quad\quad\quad \in^T = \lim_{l \to 0}(\frac{l + \Delta l}{l}) - 1$
- Logarithmic or true strain: $\quad\quad \in^l = Ln\,[\lim_{l \to 0}(\frac{l + \Delta l}{l})]$
- Green's strain: $\quad\quad\quad\quad\quad \in^G = \frac{1}{2}\,[\,(\lim_{l \to 0}(\frac{l + \Delta l}{l}))^2 - 1]$

The True strain is used in sheet metal forming and engineering analysis.

The deformation gradient is decomposed into two tensors as follow: a rotation and a stretch matrix (F = R x U). A functional connection is made between the deformation tensor F and the coordinates of the deformed and undeformed points as follows:

$P_{coordinate\ of\ the\ undeformed\ point} = U_i + F\ x\ P_{coordinate\ of\ the\ deformed\ point}$

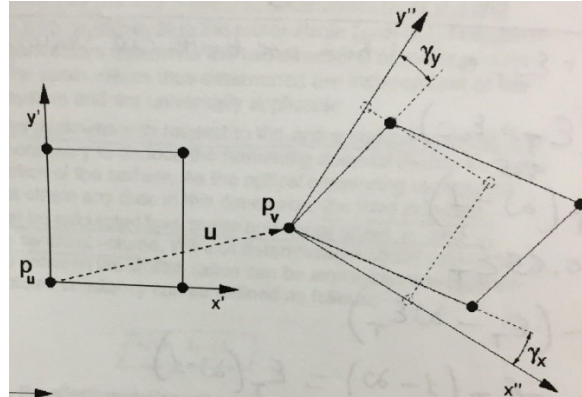where U_i is the rigid body translation tensor.

Figure 1: Translation and rotation of a point deformation

Major and minor strains are calculated based on the larger and smaller eigenvalue which can be calculated as follow:

$$\lambda_{1,2} = 1 + \frac{\epsilon_x + \epsilon_y}{2} \pm \sqrt{[(\overline{\frac{\epsilon_x + \epsilon_y}{2}})^2 - (\epsilon_x \cdot \epsilon_y - \epsilon_{xy}{}^2)]}$$

And the third principle strain can be calculated from major and minor strains assuming a constant volume.

Strain is calculated based on nodes displacement, where a pattern match is found between the deformed and undeformed node, and their coordinates are correlated to calculate the displacement at this node. The pattern is not found based on matching two speckles together, but it is based on matching light intensity over an entire field of view, and then compare intensity for two-pixel fields and calculate their displacement. Once the displacement at all nodes are calculated, the strain at each node is calculated based on displacement over a filter window which contains a group of nodes.

Figure 2: Filter window for strain calculation